

# **LLM-Powered Flood Depth Estimation from Social Media Imagery: A Vision-Language Model Framework with Mechanistic Interpretability for Transportation Resilience**

**Nafis Fuad**

Civil and Environmental Engineering  
Wayne State University  
5050 Anthony Wayne Drive, Detroit, MI, USA, 48202  
Tel: 267-446-4434; Email: [nafisfuad@wayne.edu](mailto:nafisfuad@wayne.edu)

**Xiaodong Qian**, Corresponding Author

Civil and Environmental Engineering  
Institute for AI and Data Science (AIDaS)  
Wayne State University  
5050 Anthony Wayne Drive, Detroit, MI, USA, 48202  
Tel : 313-577-3854; Email: [xdqian@wayne.edu](mailto:xdqian@wayne.edu)

## ABSTRACT

Urban flooding poses an escalating threat to transportation network continuity, yet no operational system currently provides real-time, street-level flood depth information at the centimeter resolution required for dynamic routing, electric vehicle (EV) safety, and autonomous vehicle (AV) operations. This study presents FloodLlama, a fine-tuned open-source vision–language model (VLM) for continuous flood depth estimation from single street-level images, supported by a multimodal sensing pipeline using TikTok data. A synthetic dataset of approximately 190,000 images was generated, covering seven vehicle types, four weather conditions, and 41 depth levels (0–40 cm at 1 cm resolution). Progressive curriculum training enabled coarse-to-fine learning, while LLaMA 3.2-11B Vision was fine-tuned using QLoRA. Evaluation across 34,797 trials reveals a depth-dependent prompt effect: simple prompts perform better for shallow flooding, whereas chain-of-thought (CoT) reasoning improves performance at greater depths. FloodLlama achieves a mean absolute error (MAE) below 0.97 cm and  $\text{Acc}@5\text{cm}$  above 93.7% for deep flooding, exceeding 96.8% for shallow depths. A five-phase mechanistic interpretability framework identifies layer L23 as the critical depth-encoding transition and enables selective fine-tuning that reduces trainable parameters by 76–80% while maintaining accuracy. The Tier 3 configuration achieves 98.62% accuracy on real-world data and shows strong robustness under visual occlusion. A TikTok-based data pipeline, validated on 676 annotated flood frames from Detroit, demonstrates the feasibility of real-time, crowd-sourced flood sensing. The proposed framework provides a scalable, infrastructure-free solution with direct implications for EV safety, AV deployment, and resilient transportation management.

*Keywords: Flood depth estimation, Vision–language models, Transportation resilience, Social media sensing, Large-Language Model (LLM)*

## INTRODUCTION

Urban flooding has become one of the most disruptive hazards to transportation systems, driven by climate change, aging drainage infrastructure, and increasing urbanization. In the United States, flood-related damages to transportation infrastructure amount to billions of dollars annually, including both direct physical damage and indirect impacts such as travel delays, freight disruption, and emergency response costs. Existing infrastructure, often designed for outdated rainfall conditions, is increasingly unable to accommodate modern storm intensities, leading to more frequent and severe urban flooding events.

A critical limitation in current transportation systems is the lack of real-time, street-level flood-deep information. Navigation platforms such as Google Maps and Waze rely primarily on binary road-closure reports, which are often delayed and lack depth-specific information. However, flood impacts on transportation are highly sensitive to depth: small increases in water

level can lead to disproportionate reductions in network connectivity and functionality (Pregolato et al., 2017; Wang et al., 2019; Dong et al., 2022). Moreover, these disruptions propagate beyond flooded areas, affecting system-wide performance and disproportionately impacting vulnerable populations (Kasmalkar et al., 2020; Yao et al., 2024).

The need for high-resolution flood depth data is further intensified by emerging vehicle technologies. Electric vehicles (EVs) contain underbody battery systems that are sensitive to water ingress at depths of approximately 15–25 cm, requiring precise depth estimation for safe operation. Similarly, autonomous vehicles (AVs) lack robust perception mechanisms for flooded road conditions, and such scenarios are typically excluded from their operational design domains. These limitations highlight the need for centimeter-level flood depth estimation to support safe and adaptive transportation systems.

Recent advances in social media sensing provide a promising alternative to traditional monitoring approaches. User-generated content has been shown to enable near real-time detection of transportation disruptions (Gu et al., 2016; Cervone et al., 2016). However, most prior work relies on text-based platforms and does not fully utilize the rich visual and multimodal information available in video-based platforms such as TikTok. The widespread use of smartphones has effectively created a distributed sensing network capable of capturing flood conditions at high spatial and temporal resolution.

Despite this potential, several key gaps remain. Existing computer vision approaches typically provide coarse categorical depth estimates (e.g., tire or bumper level) rather than continuous measurements. Vision–language models (VLMs) applied to this problem have limited accuracy and lack interpretability, while no publicly available dataset supports centimeter-level supervised learning. Additionally, mechanistic understanding of how VLMs encode depth information remains largely unexplored, limiting opportunities for efficient model design.

To address these challenges, this study proposes an end-to-end vision–language framework for real-time flood depth estimation from social media imagery. The contributions are fourfold. First, a multimodal TikTok-based data pipeline is developed for urban flood sensing. Second, a large-scale synthetic dataset is constructed to enable centimeter-resolution training. Third, FloodLlama, a fine-tuned vision–language model, achieves sub-centimeter accuracy in flood depth estimation. Fourth, a mechanistic interpretability framework is introduced to guide selective fine-

tuning, reducing trainable parameters by 76–80% while maintaining high performance. Together, these contributions establish a scalable, infrastructure-free approach to real-time flood monitoring, with direct implications for transportation resilience, EV safety, and AV deployment in flood-prone urban environments.

## **LITERATURE REVIEW**

This section reviews six interconnected streams of literature that frame the contribution of the present study. It first discusses the vulnerability of transportation networks to flood events and the growing role of social media as a complementary sensing infrastructure for transportation applications. It then examines computer vision and deep learning approaches for flood depth estimation, followed by recent developments in vision–language models (VLMs) for transportation sensing. The section also considers the use of synthetic data to address labeled-data scarcity in safety-critical transportation tasks and highlights the increasing demand for explainable and mechanistically interpretable AI in transportation decision-making. Finally, it synthesizes the remaining research gaps and situates the present study within this context.

### **Flood Impact on Transportation Systems**

Transportation networks serve as the circulatory system of modern cities, and their disruption during flood events has cascading socioeconomic consequences that extend far beyond the physically inundated area. Research indicates that even minor, localized flooding can lead to significant network-wide failures. Dong et al. (2022) showed, through network percolation analysis of Harris County during Hurricane Harvey, that merely 2.2% of flood-induced compound failures led to a 17.7% reduction in the size of the network’s giant component, underscoring how indirect effects such as traffic rerouting and congestion amplify the direct impact of road closures. Similarly, Wang et al. (2019) developed a three-dimensional flood–road failure model and applied it to large-scale road networks in China and the United States. Their analysis revealed a discontinuous percolation transition, whereby gradual increases in flood intensity can trigger abrupt network fragmentation once a critical threshold is reached. Pregnolato et al. (2017) examined the effects of floodwater depth on road transport by proposing a depth–disruption function that relates water depth to traffic disruption. At the urban scale, Kasmalkar et al. (2020) combined traffic models with flood maps for the San Francisco Bay Area and showed that flood-

induced travel delays can propagate far beyond inundated areas. Their results indicate that local road network structure, measured by metric reach, influences vulnerability more strongly than direct flood exposure, emphasizing the need for real-time, spatially resolved flood depth information to support dynamic routing (Jenelius, 2010). Yao et al. (2024) examined flood impacts on automobile commuters in Shanghai under sea-level-rise scenarios and found that long-distance and lower-income commuters face greater disruption, while increasing sea levels gradually reduce commuting resilience across all groups. Shahdani et al. (2022) used mesoscopic traffic simulation in Portugal, to study flood impacts and showed that coupled flood–traffic models can capture disruption propagation and lingering traffic congestion even after floodwaters recede. (Marian et al., 2024) further advanced this work by using microscopic simulations of flood-related road closures in Qatar to quantify vulnerability at both component and network levels. These studies highlight that effective flood impact assessment requires both inundation extent and detailed depth information to support real-time decisions on partial closures and speed reductions.

Despite these advances, a significant gap remains in the operational availability of real-time flood depth data at the street level. Most existing approaches rely on hydrological models, satellite imagery, or post-event surveys—none of which can provide the minute-by-minute, road-segment-level depth information needed for integration with real-time navigation platforms such as Google Maps or Apple Maps. This gap motivates the exploration of alternative data sources, particularly social media imagery, which is the subject of the next section.

### **Social Media Data Mining for Transportation Applications**

The recognition that social media users function as ubiquitous, low-cost sensors has transformed transportation research over the past decade. Gu et al. (2016) showed that Twitter data can detect traffic incidents in near real time across highways and arterials in Pittsburgh and Philadelphia, providing broader spatial coverage than traditional detectors. Their framework combined keyword filtering, natural language processing based geocoding, and deep belief network classification, and has since guided many subsequent studies. Social media has become an important information source during disaster events, particularly when traditional sensing infrastructure is damaged or overloaded. Cervone et al. (2016) demonstrated that integrating Twitter and Flickr data with satellite imagery during the 2013 Colorado floods enabled the identification of flooding hotspots that were not detected using satellite imagery alone, highlighting the complementary value of

crowdsourced visual data. Reynard & Shirgaokar (2019) analyzed geolocated tweets during Hurricane Irma in Florida and used a multinomial logit model to identify tweet, user, and location features associated with negative sentiments about damage and transportation disruption. Their study shows that social media can provide both spatial and attitudinal insights for disaster response. Social media-based transportation event detection has evolved from text-only analysis to multimodal approaches that integrate images and videos. For example, Ali et al. (2021) reported that deep learning models combining word embeddings with bidirectional LSTM networks achieved over 97% accuracy in detecting traffic events and conditions from social media text. In parallel, disaster management research has developed frameworks to extract actionable information from social media during emergencies, using BERT-based models and geospatial clustering to classify damage, rescue needs, and infrastructure conditions (L. Huang et al., 2021).

However, a critical observation in this literature is the dominance of Twitter/X as the platform of study and the reliance on text-based analysis. Relatively few studies have explored video-centric platforms such as TikTok, which offer several advantages for flood monitoring: (a) inherently visual and video-based content providing richer spatial information, (b) a younger and more geographically diverse user base, (c) geotagging and hashtag-based discoverability, and (d) audiovisual metadata including speech content and ambient sounds that may contain contextual flood information. The present study addresses this gap by developing a TikTok-based data collection pipeline that extracts not only visual frames but also audio transcriptions, captions, and user engagement signals, establishing a multimodal data foundation for flood depth estimation.

### **Computer Vision and Deep Learning for Flood Depth Estimation**

While many studies focus on binary flood detection using CNNs and transfer learning (Hussain et al., 2024; Sazara et al., 2019) or pixel-level flood extent mapping with semantic segmentation models such as U-Net and DeepLabV3+ (Chen et al., 2018; Zeng et al., 2024), this study addresses the more challenging task of estimating flood depth at centimeter-level resolution from street-level images. Existing research in flood depth estimation has evolved through three main approaches: reference-object geometric methods, object detection-based depth classification, and recent large multimodal model approaches. Early image-based flood depth estimation methods relied on detecting partially submerged objects of known dimensions and estimating depth through geometric reasoning using reference objects such as traffic signs, barrels, and staff gauges.

(Alizadeh Kharazi & Behzadan, 2021; Jafari et al., 2021; Jiang et al., 2019). Among these, traffic signs and pedestrians were initially the most investigated. Alizadeh Kharazi & Behzadan (2021) estimated street-level flood depth from crowdsourced images of submerged stop signs using a CNN-based traffic sign detector and visible pole length comparison, achieving a mean absolute error of about 12 cm and introducing a tilt-correction method for improved accuracy. Vallimeena et al. (2018) introduced a flood monitoring system that uses the average human height as a reference, classifying faces by gender and age group to select appropriate height priors for depth calculation. However, these reference-object-based approaches face fundamental scalability limitations. Liu et al. (2025) note that methods relying on reference objects such as stop signs or barrels are not consistently applicable because these objects are not always visible in images. Pedestrians also present challenges due to low resolution, variable posture, and reduced presence during severe flooding (Qiu et al., 2025). These limitations have led to vehicle-based approaches, as vehicles are more commonly present, have stable shapes, and remain visible even in moderate flooding. Vehicles have become the dominant reference objects for image-based flood depth estimation due to advances in object detection models. Park et al. (2021) used Mask R-CNN to detect submerged vehicles and combined it with VGGNet based matching of 3D rendered vehicle features for depth estimation. Huang et al. (2020) also applied Mask R-CNN to detect vehicle wheels and classify flood depth based on wheel submersion. The YOLO family has further advanced this approach. Zhong et al. (2024) used YOLOv4 to detect submerged reference objects and found vehicles provided higher depth estimation accuracy than pedestrians. Building on this, Liu et al. (2024) introduced the BEW-YOLOv8 model with BiFPN, EffectiveSE, and WIoU modules to improve multi scene flood depth detection. Qiu et al. (2025) later developed a YOLOv8 based system using buses as reference objects, noting that buses provide more consistent height references than cars, whose varying dimensions limit their usefulness once fully submerged. Studies have moved toward end-to-end deep learning pipelines that combine detection, estimation, and geospatial mapping. Notarangelo et al. (2025) proposed STURM-FloodDepth, which integrates vehicle detection, image enhancement, flood level classification, and georeferencing to map urban flood depths from street level and aerial imagery, exporting results for GIS analysis, although depth is still treated as a discrete classification task. Hao et al. (2022) estimated spatial and temporal variations in street flooding from surveillance videos by tracking water levels relative to fixed reference points, but the method is limited to fixed camera settings and does not generalize

well to diverse social media imagery. Recent research in flood depth estimation has explored large multimodal models (LMMs) capable of jointly processing visual and textual information. Akinboyewa et al. (2024) introduced FloodDepth-GPT, which uses GPT-4 Vision to estimate flood depth from images containing reference objects such as cars, signs, and buildings, achieving a Pearson correlation of  $r = 0.8879$  and an MAE of 25 cm without task-specific training. Lyu et al. (2025) evaluated several LMMs, including GPT-4, Gemini, and LLaVA, against a YOLOv5 baseline for urban flood depth estimation, finding that GPT-4 achieved the highest average accuracy (58.8%) and that performance depends strongly on the alignment between prompt complexity and visual content. Liu et al. (2025) further proposed FloodVision, a zero-shot framework combining GPT-4o with a domain knowledge graph of urban object dimensions, achieving an MAE of 8.17 cm on crowdsourced flood images and outperforming both the GPT-4o baseline and earlier CNN-based methods.

Despite the rapid progress reviewed above, several critical gaps remain that the present study addresses. First, all existing vehicle-centric methods treat flood depth as a discrete classification problem with coarse categories (e.g., tire-level, bumper-level, door-level), rather than as a continuous variable at centimeter resolution. Second, the LMM-based approaches (FloodDepth-GPT, FloodVision) rely on zero-shot prompting of proprietary models without task-specific fine-tuning, resulting in inconsistent outputs and MAEs that remain above 8 cm even in the best cases. Third, no prior study has fine-tuned an open-source VLM specifically for flood depth estimation, which would enable both reproducibility and the mechanistic interpretability analysis needed for safety-critical transportation deployment. Fourth, the training data challenge remains unresolved: there is no publicly available dataset pairing street-level flood images with centimeter-resolution depth labels across diverse vehicle types, weather conditions, and traffic compositions. The present study addresses all four gaps by: (a) generating a comprehensive synthetic dataset at 1 cm depth increments across 7 vehicle types and 4 weather conditions; (b) fine-tuning an open-source VLM (Llama 3.2 Vision) for continuous flood depth estimation; (c) investigating prompt strategies that optimize cross-attention alignment; and (d) conducting the first mechanistic interpretability analysis of a flood depth estimation model.

## **Vision-Language Models in Transportation Sensing**

Vision language models (VLMs) have shifted computer vision from task specific models to general multimodal systems capable of jointly interpreting images and text. The release of CLIP (Radford et al., 2021), trained on 400 million image text pairs, enabled zero shot visual recognition through natural language prompting, and later models such as LLaVA, Flamingo, and Llama 3.2 Vision extended this capability by integrating vision encoders with large language models. Transportation research has begun exploring these models; for example, Prajapati et al. (2024) evaluated several VLMs for tasks such as congestion detection, pavement crack identification, and helmet violation detection, while Zhang & Liu (2025) proposed DamageQwen for pavement damage detection with minimal training data. VLMs are also gaining traction in autonomous driving and intelligent transportation systems for tasks including scene understanding and decision making (Song et al., 2026; Zhou et al., 2024), and have been applied to infrastructure monitoring such as vehicle classification from LiDAR data (Li et al., 2026). However, their use in flood related transportation analysis remains limited. Flood depth estimation from street level imagery requires reasoning over both visual cues and contextual knowledge, making it well suited to multimodal approaches. To the best of our knowledge, this study is the first to fine tune a VLM (Llama 3.2 Vision) for centimeter level flood depth estimation from street level images and to investigate its mechanistic interpretability in a transportation safety context.

## **Synthetic Data Generation for Transportation Safety Applications**

Synthetic data has become a widely used solution for training data scarcity in autonomous driving and transportation safety research. Real world data collection for safety critical scenarios is costly, limited, and often lacks rare events. Driving simulators such as CARLA and VISTA 2.0 show that models trained on synthetic data can transfer to real environments when the simulated data captures realistic visual and physical characteristics (Dosovitskiy et al., 2017). Synthetic data is also used to address the long tail distribution of rare but critical scenarios such as extreme weather and near collisions. For example, Kim et al. (2025) introduced SynAD to improve autonomous driving models using synthetic multi agent scenarios, while (Tamayo-Urgilés et al., 2024) used GAN generated driving events for accident risk classification with performance comparable to real data training. Synthetic imagery has also supported transportation safety tasks such as safe distance classification and crash scenario simulation (Shitala Prasad et al., 2026). These approaches are

particularly useful when labeled data is scarce, when continuous variables require fine resolution, and when controlled conditions are needed for model evaluation. All these conditions apply to flood depth estimation, where no public dataset links street level flood images with centimeter level depth labels. Because real flood events are unpredictable and involve many uncontrolled variables, this study generates a synthetic dataset covering multiple vehicle types, weather conditions, and flood depths from 0 to 40 cm at 1 cm increments to support fine grained flood depth estimation from street level imagery. Sazara et al. (2022) also developed deep learning based model trained on combination of real-world flood images and synthetically generated flooded street images created with the Unity simulation platform.

### **Explainable AI and Mechanistic Interpretability in Transportation Models**

The growing use of deep learning in safety critical transportation systems has increased the need for explainable and interpretable models. In transportation research, explainable AI methods such as SHAP and LIME have been widely used to interpret models for crash prediction and travel demand analysis (Abdulrashid et al., 2025). However, these approaches mainly provide post hoc explanations of model outputs. Mechanistic interpretability instead focuses on understanding the internal computational processes of neural networks (Bereska & Gavves, 2024). While explainability techniques have been applied to autonomous driving perception systems (Kim et al., 2018), their use in transportation safety models remains limited. This study addresses this gap by applying mechanistic interpretability methods to a vision language model fine-tuned for flood depth estimation through layer-level ablation of cross-attention mechanisms, linear probing for task-specific information decoding, logit lens analysis of visual-to-language alignment, centered kernel alignment for representational divergence tracking, or causal attention blocking validation.

### **Research Gaps and Contribution**

Prior studies show that flooding can severely disrupt transportation networks, yet no operational system provides real-time, street-level flood depth information at the resolution required for navigation platforms. Social media videos offer rich real-time flood observations but remain underused beyond text-based analyses. Existing computer vision approaches rely on limited reference objects or classify flood depth into coarse categories, while recent multimodal models operate in zero-shot settings without training transparency or consistent accuracy. In addition, no

public dataset links street-level flood images with centimeter-level depth labels, and mechanistic interpretability has not been explored in transportation safety models.

To address these gaps, this study develops an end-to-end framework that converts social media video into centimeter-level flood depth estimates. The framework includes a TikTok-based multimodal data pipeline, a synthetic dataset covering multiple vehicle types, weather conditions, and flood depths, and a fine-tuned vision-language model (Llama 3.2 Vision) for continuous flood depth estimation. The study further analyzes prompt strategies and applies mechanistic interpretability techniques to reveal internal model behavior, enabling selective fine-tuning with significant parameter reduction while maintaining performance.

## **RESEARCH FRAMEWORK**

Figure 1 presents the proposed multimodal framework for flood depth estimation from social media videos. The pipeline begins with data collection from TikTok, where video frames, on-screen text extracted via optical character recognition (OCR), speech transcripts obtained through automatic speech recognition (ASR), and user comments are retrieved. The visual stream processes extracted video frames through a flood-versus-non-flood detection module to filter relevant flood scenes. Identified flood images are then analyzed using the proposed FloodLlama vision–language model to estimate flood depth from visual cues. In parallel, the textual stream processes speech, OCR text, and social media comments using the Llama 3.2 language model to extract contextual and subjective information related to the flood event. A location estimation algorithm utilizes textual and metadata information to infer the geographical flood area. By integrating visual depth estimation with contextual and spatial information from multimodal sources, the framework enables comprehensive flood characterization from social media content. For this study, flooded-road-related TikTok videos and associated metadata were collected from Detroit as a sample city; however, the proposed methodological framework is applicable worldwide.

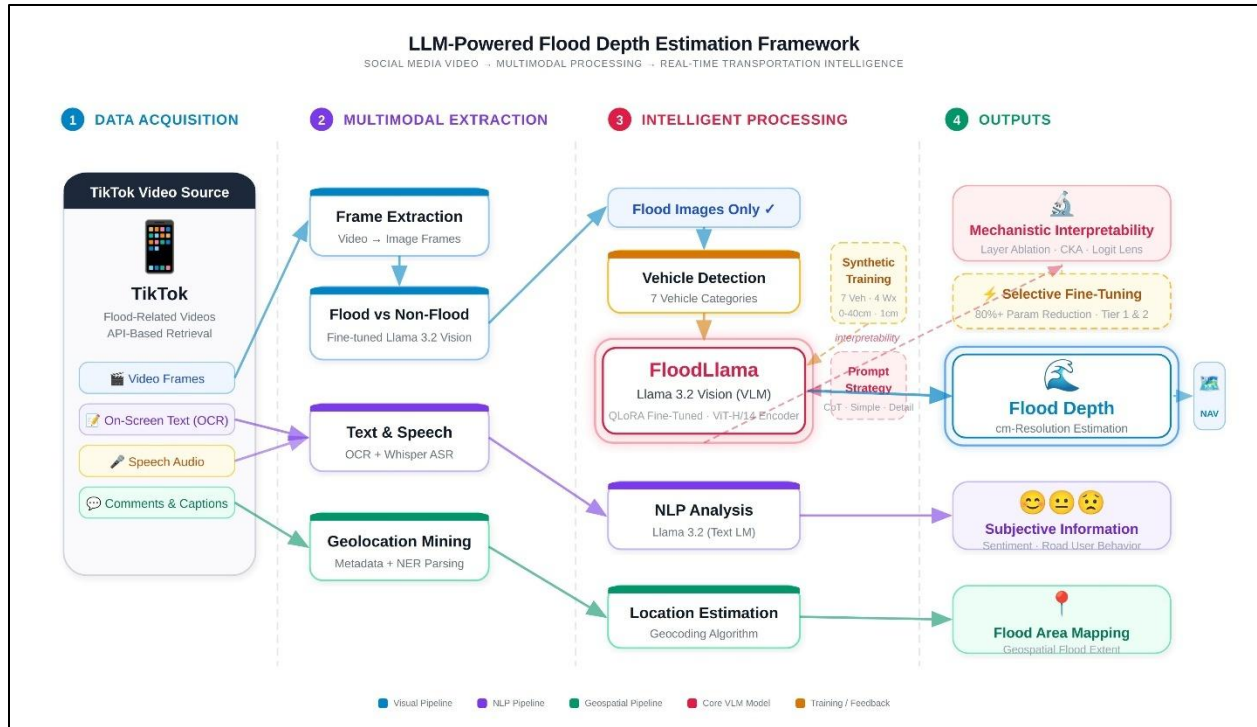


Figure 1. The proposed multimodal pipeline for flood depth estimation using TikTok video, text, and audio data.

### TikTok Video Acquisition Pipeline

Data acquisition follows a three-phase pipeline: (1) programmatic data collection using the TikTok Research API to retrieve videos, metadata, and comments; (2) visual preprocessing including frame extraction, and perceptual deduplication; and (3) multimodal text extraction using OCR and ASR. Detroit-focused queries (2016–2025) using keywords and hashtags such as *Detroit Flooding* and *Flooded Detroit* were used to capture flood-related content. SHORT-format videos were excluded to retain sustained flood footage. The API was queried with pagination to collect all results, and duplicate video IDs were removed. The final dataset includes 676 unique flood frames, 28,370 viewer comments, OCR-extracted text, and audio transcriptions.

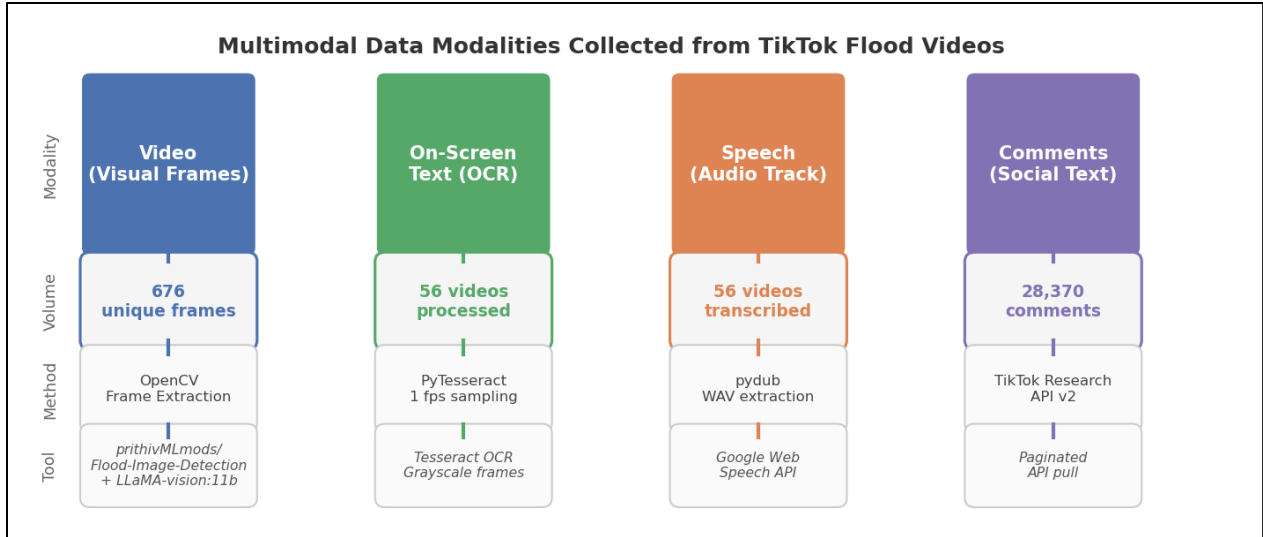


Figure 2. The summary of the four multimodal data streams collected from each TikTok flood video.

### Flood Scene Classification

Accurate flood depth estimation from roadway images first requires determining whether the scene is flooded or not. This task is addressed through a fine-tuned vision-language model for flood detection. Flood scene detection is formulated as a binary image classification task in which a vision–language model classifies images as flooded or non-flooded using natural language prompts and visual context. The flood detection dataset was open sourced having 13,485 RGB images with a class imbalance (flood: non-flood = 2.6:1), reflecting realistic flood-event imagery distributions.

Table 1. The flood detection dataset composition.

Split	Flood	Non-Flood	Total
Training (fine-tuning)	9,737	3,748	13,484
Test (evaluation)	441	1,380	1,821
Total	10,178	5,128	13,485

A zero-shot baseline was established using LLaMA 3.2-11B Vision Instruct with the prompt: “Does this image depict flooding? Respond with exactly 1 for flood, 0 for non-flood.” The model was evaluated on 13,485 images, producing 13,393 valid predictions. Results show strong precision for flood detection (0.98) but lower recall (0.74), indicating the model tends to conservatively classify ambiguous scenes as non-flooded, leading to many missed flood cases. Overall, zero-shot accuracy was 79.96%.

To improve performance, the model was fine-tuned using Supervised Fine-Tuning (SFT) with LoRA through the Unsloth framework. Only 0.63% of parameters (67.2M of 10.74B) were trainable using LoRA ( $r=16$ ,  $\alpha=16$ ) with 4-bit NF4 quantization. Training used 11,664 images, a batch size of 8 (effective), 2 epochs, and 3,372 optimization steps on an NVIDIA RTX 4090, requiring approximately 10.3 hours. The fine-tuned model achieved 99.73% accuracy on the 1,821-image test set with only five misclassifications and no invalid outputs, improving performance by 19.77 percentage points over the zero-shot baseline (Figure 3 and Table 2). The final training loss of 0.00609 indicates near-complete convergence on the training set.

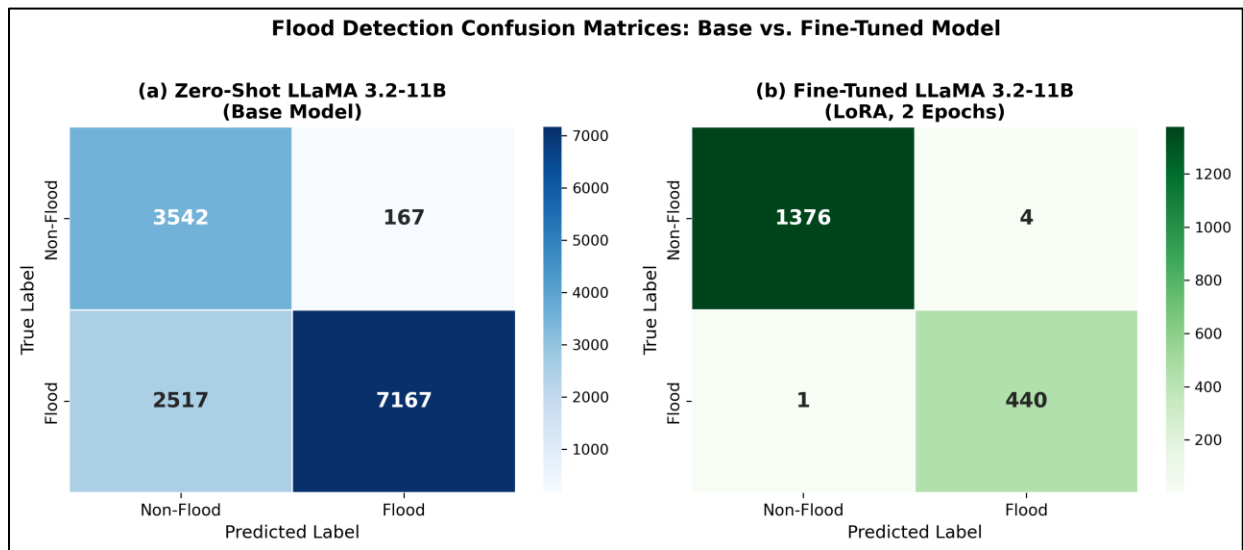


Figure 3. The flood detection confusion matrices: (a) zero-shot LLaMA 3.2-11B baseline; (b) fine-tuned LLaMA 3.2-11B with LoRA (2 epochs).

Table 2. The comparison summary of flood scene detection.

Model	Accuracy	Macro F1	Non-Flood F1	Flood F1	Invalid Resp.
LLaMA 3.2-11B (Zero-Shot)	79.96%	0.78	0.73	0.84	0.68%
LLaMA 3.2-11B (Fine-Tuned)	99.73%	1.00	1.00	0.99	0.00%
Improvement	+19.77 pp	+0.22	+0.27	+0.15	—

## Vehicle Type Classification

Flood depth estimation from vehicle shapes requires knowledge of vehicle geometry, including ground clearance and body dimensions, which vary across vehicle types. To obtain this information, we treat vehicle identification as a fine-grained image classification task using the Stanford Cars Dataset, consisting of 196 make–model–year categories spanning sedans, SUVs,

pickups, vans, and other body styles relevant to flood depth assessment. The Stanford Cars Dataset contains 16,185 images across 196 vehicle categories, split into 6,515 training, 1,629 validation, and 8,041 test images. The training set shows near-uniform class distribution ( $IR = 2.84$ ,  $Gini = 0.051$ ), making it suitable for standard cross-entropy training without class-weighted loss. For flood scene detection, fine-tuning LLaMA 3.2-11B Vision Instruct with LoRA on 13,484 images for two epochs achieved 99.73% test accuracy, improving the zero-shot baseline by 19.77 percentage points and reducing the flood-class false negative rate from 26% to below 0.23%. For vehicle type classification, a ResNet-50 baseline trained on the 196-class Stanford Cars Dataset achieved 82.50% top 1 validation accuracy. Together, these models provide reliable scene understanding for the subsequent VLM-based flood depth estimation pipeline.

After identifying flood scenes and vehicle type from flood images, flood depth estimation process starts. The remainder of the paper focuses on the development of the flood depth estimation model, including dataset preparation, model fine-tuning, and mechanistic interpretability analysis. Insights from the interpretability study are further used to design more efficient training and inference strategies.

## **SYNTHETIC FLOOD IMAGE GENERATION FOR DEPTH-LABELED TRAINING**

Training flood depth estimation models is constrained by the lack of real images with precise depth labels. To address this, we developed a synthetic data generation pipeline using Unreal Engine 5, a photorealistic simulation platform widely used in autonomous driving research (Epic Games, 2022). The simulated environment replicates urban roadway scenes with realistic textures, buildings, markings, and physically simulated floodwater. Seven vehicle types were placed at controlled positions while flood depth was programmatically varied at centimeter resolution, under four lighting conditions (sunny, afternoon, night, and rainy). The resulting dataset contains over 1.7 million single-vehicle images and 1.08 million mixed-vehicle scenes, providing accurate ground truth and scalable training data for flood depth estimation.

### **Single-Vehicle Synthetic Dataset**

The single-vehicle synthetic dataset was generated by systematically varying three primary factors: flood depth, vehicle type, and weather condition. Flood depth was sampled at nine discrete levels spanning the operational range of the depth estimation pipeline: 0, 5, 10, 15, 20, 25, 30, 35, and

40 cm. Seven vehicle types were included: BUS, Trailer, and VAN (categorized as Big Vehicles); SUV, Truck, and Mini van (Medium Vehicles); and Sedan (small vehicle). Detailed vehicle dimensions are given in Table 3. All four weather conditions (Afternoon, Night, Rainy, Sunny) were applied to every depth-vehicle combination, yielding a fully crossed experimental design.

Table 3. The vehicle type and physical dimension of synthetic dataset.

Vehicle Type	Group	Height Side (cm)	Height Front (cm)	Tire Height (cm)	Ground Clearance (cm)	Count
BUS	Big Vehicle	303	306	94	18	83,994
Trailer		400	400	98	42	87,788
VAN		254	254	76	28	76,453
SUV	Medium Vehicle	176	176	70	24	134,606
Truck		184	184	79	28	103,662
Mini van		186	186	72	17	101,060
Sedan	Sedan	150	150	63	14	137,808

Table 4 shows the distribution of single-vehicle dataset. Each image in the single-vehicle dataset includes structured metadata such as file path, weather condition, vehicle type, vehicle dimensions, and flood depth, all generated directly from simulation parameters to ensure zero labeling error. These annotations enable ratio-based depth estimation by linking predicted depth with vehicle geometry to compute metric flood depth.

Table 4. The synthetic single-vehicle dataset distribution.

Category	Subcategory	Big Vehicle	Medium Vehicle	Sedan	Total (%)
Flood Depth (cm)	0 (No Flood)	81,243	77,523	29,550	11.8
	5	16,190	18,154	5,813	10.6
	10	131,628	275,154	151,293	13.9
	15	80,172	110,457	43,689	11.9
	20	89,472	113,928	38,613	12.4
	25	79,104	118,386	36,642	12.1
	30	47,373	46,596	12,317	10.4
	35	26,410	25,769	10,518	10.3
	40 (Deep Flood)	22,319	28,168	9,231	10.6
<b>Weather Distribution</b>					
	Rainy				27.6%
	Night				25.3%
	Sunny				23.6%
	Afternoon				23.5%

### Mixed-Vehicle Synthetic Dataset

The single-vehicle dataset contains only one vehicle per image, whereas real flood scenes often include multiple vehicles, which can create occlusions and increase visual complexity. To better reflect these real-world conditions and improve model generalization, a mixed-vehicle dataset was generated in Unreal Engine 5 with multiple vehicles placed within each scene. This data set

provides continuous flood depth labels from 1 to 40 cm at 1 cm intervals and contains 1,082,018 images (Table 5).

*Table 5. The mixed-vehicle dataset with weather condition distribution.*

<b>Weather</b>	<b>Image Count</b>	<b>Percentage (%)</b>
Rainy	349,876	32.3
Sunny	349,548	32.3
Afternoon	234,400	21.6
Night	148,194	13.7

Table 6 provides a consolidated summary of both synthetic datasets. The combined corpus totals 2,810,930 images with full depth labels, encompassing seven vehicle groups (or mixed multi-vehicle scenes), four weather conditions, and depth values from 0 to 40 cm. The scale and annotation completeness of this corpus substantially exceeds any existing publicly available flood depth dataset. Figure 4 shows the sample images under each category of synthetic data.

*Table 6. The Combined synthetic dataset summary.*

<b>Dataset</b>	<b>Depth Levels</b>	<b>Vehicle Types</b>	<b>Weather</b>	<b>Total Images</b>	<b>Annotation</b>
Single-Vehicle (UE5)	9 discrete (0–40 cm)	BUS, Trailer, VAN, SUV, Truck, Mini-van, Sedan	4	1,725,712	Full metadata CSV
Mixed-Vehicle (UE5)	40 continuous (1–40 cm)	Multiple vehicles per scene	4	1,085,218	Depth + Weather CSV
Combined Total	0–40 cm	7 types + multi-vehicle	4	2,810,930	Fully labeled

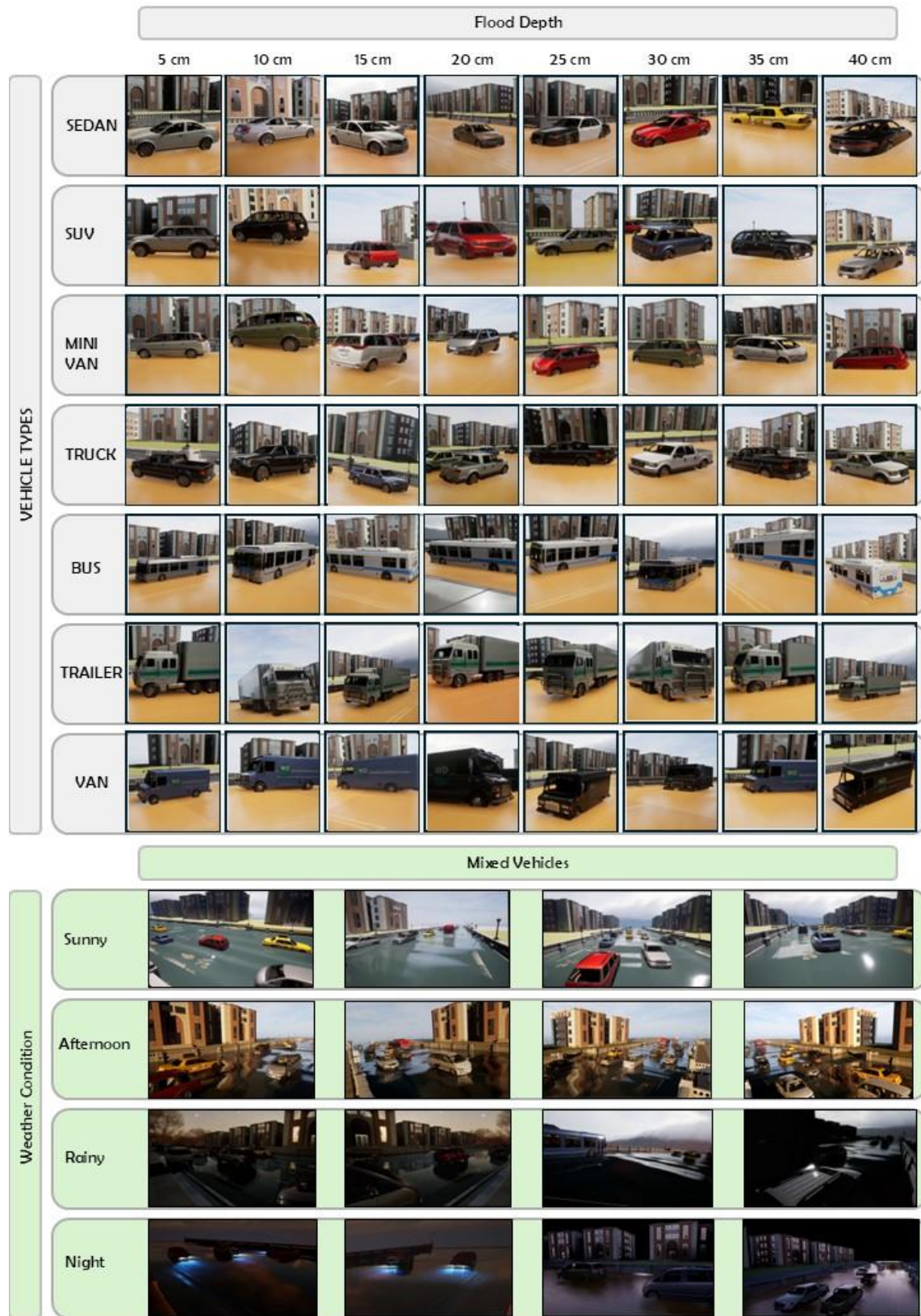


Figure 4. The synthetic images by category in the flood depth estimation dataset.

## Realism Assessment: Synthetic vs. Real-World Imagery

A persistent challenge in sim-to-real transfer learning is the visual domain gap between synthetic and real imagery. To quantify the visual fidelity of the UE5-generated flood scenes relative to real-world flood photographs, we conducted a realism assessment: a pixel-level statistical analysis comparing intensity distributions, color channel means, saturation, and contrast across 600 randomly sampled images from each domain. Pixel-level analysis compared 600 images each from three sources: real flood images (sampled from the image corpus in Flood scene classification), single-vehicle synthetic images, and mixed-vehicle synthetic images. All images were resized to 224×224 pixels, and statistical similarity was evaluated using the Kolmogorov–Smirnov (KS) two-sample test, where lower KS values indicate greater distributional similarity.

Table 7 summarizes the mean pixel statistics across the three image domains. The single-vehicle synthetic images are systematically darker (mean brightness 86.3) compared to real flood images (mean brightness 120.4), reflecting the controlled indoor-style lighting and shadow-heavy UE5 rendering environment. The mixed-vehicle images exhibit intermediate brightness (102.1), suggesting improved calibration in the second-generation simulation setup. In contrast, saturation is significantly higher in synthetic images (73.3 for single-vehicle, 52.0 for real), consistent with the more vivid and spectrally pure colors typical of game-engine rendering.

Table 7. The pixel-level statistics comparison — real vs. synthetic flood images ( $n=600$  each).

Metric	Real Flood	Synthetic (Single-Veh)	Synthetic (Mixed-Veh)
Mean Brightness	120.4	86.3	102.1
Mean Saturation	52.2	73.3	52.0
Contrast (Std)	56.2	59.3	55.8
Mean R Channel	121.2	94.1	107.3
Mean G Channel	123.5	84.3	103.8
Mean B Channel	113.6	78.8	95.0

The KS analysis (Table 8) reveals that the mixed-vehicle dataset achieves substantially better alignment with real flood images for brightness (KS=0.308 vs 0.445) and saturation (KS=0.167 vs 0.443). These improvements reflect iterative scene calibration in the second-generation UE5 environment. The contrast distribution shows comparable KS statistics across both synthetic configurations (0.235 and 0.327), suggesting that textural variation and detail complexity are similarly rendered in both datasets. The domain gap between UE5 synthetic and real flood images mainly arises from brightness and color differences due to rendering and illumination variations. However, contrast distributions are closely matched (KS = 0.235), indicating similar

spatial texture complexity. This is important because flood depth cues, such as waterline position, tire submersion, and reflections, depend more on texture than brightness.

Table 8. The Kolmogorov Smirnov statistics — pixel feature similarity to real flood images (lower = more similar).

Feature	KS: Real vs Single-Veh Syn	KS: Real vs Mixed-Veh Syn
Brightness	0.445	0.308
Saturation	0.443	0.167
Contrast	0.235	0.327
R Channel	0.382	0.251
G Channel	0.421	0.282
B Channel	0.413	0.271

## FINE-TUNING LLAMA 3.2 VISION FOR FLOOD DEPTH ESTIMATION

This section describes the fine-tuning of LLaMA 3.2-11B Vision Instruct for flood depth estimation from monocular street images. Vision–language models were selected for their ability to jointly interpret visual cues and contextual knowledge, enabling more robust scene understanding than traditional CNN-based approaches. LLaMA 3.2 Vision was chosen for its strong multimodal reasoning capability, open-weight availability, and compatibility with parameter-efficient fine-tuning (Meta AI, 2024). Before fine-tuning, several open-source vision–language models were evaluated, including DeepSeek 3B, LLaMA 3.2 Vision-11B, Qwen-3-7B, and LLaVA-13B. Among them, LLaMA 3.2 Vision-11B achieved the best baseline performance. Using different prompt designs and image inputs, the foundational model reached an  $R^2$  of 0.612, which was the highest among the tested models but still insufficient for reliable flood depth estimation, motivating further fine-tuning.

### Model Architecture

LLaMA 3.2-11B Vision Instruct is a decoder-only multimodal model that processes image–text pairs through a cross-modal adapter linking a pretrained vision encoder to the language backbone (Figure 5). During fine-tuning, the vision encoder and cross-modal projector remain frozen, while the language model parameters are adapted using Low-Rank Adaptation (LoRA). This strategy preserves pretrained visual representations while enabling efficient task-specific adaptation of the reasoning and output layers. LoRA parameterizes each weight matrix  $W$  as  $W + BA$ , where  $A$  and  $B$  are low-rank matrices with rank  $r = 16$  and scaling factor  $\alpha = 16$ . The adapters are applied to the query, key, value, and output projection layers of the attention modules. With 4-bit NF4

quantization of the frozen base weights, only 52.4 million parameters (0.49% of 10.72B) remain trainable, allowing the model to be fine-tuned efficiently on a single 24 GB GPU.

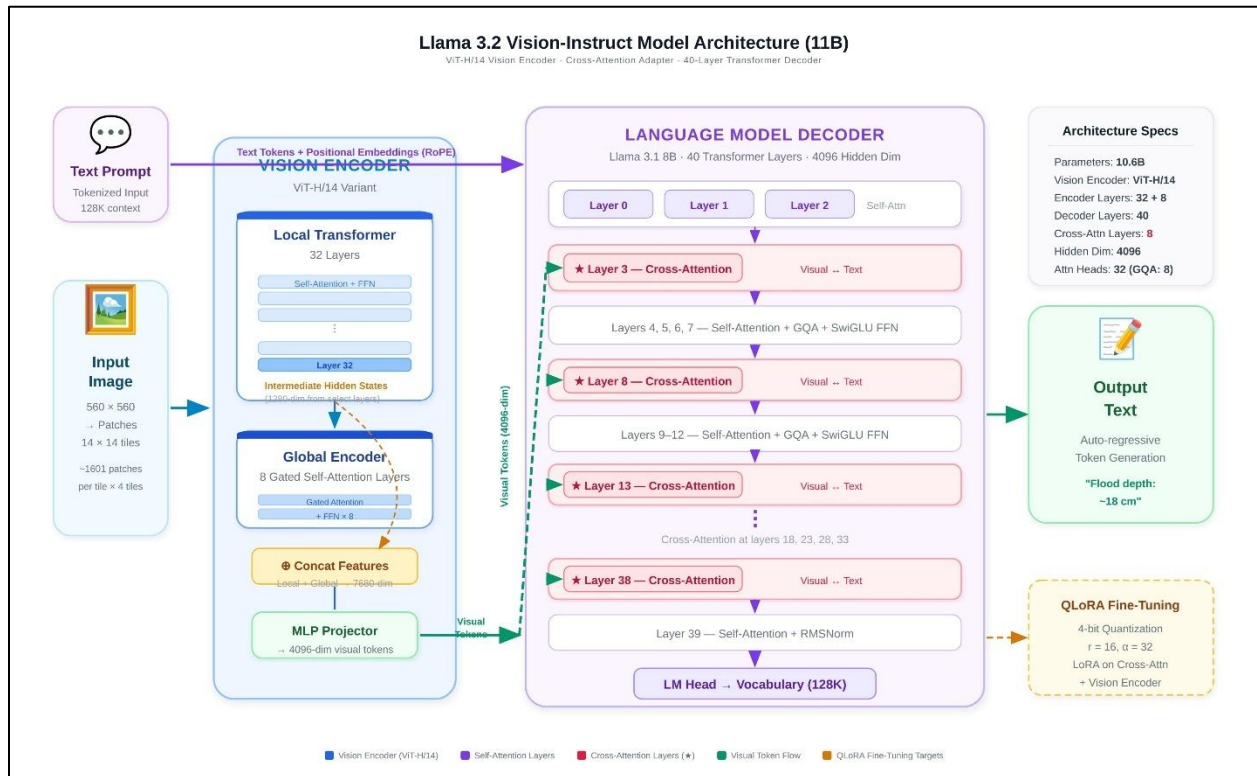


Figure 5. The architecture of LLaMA 3.2 vision foundational model.

## Structured Prompt Design for Fine-Tuning

A critical design choice for the fine-tuning objective is the construction of the input prompt and the expected output schema. Since flood depth is not directly recoverable from image pixels alone without prior knowledge of vehicle geometry, the prompt provides the model with structured metadata as auxiliary cues. Specifically, for each training image the prompt includes: (1) the tire height in centimeters, (2) the ground clearance of the target vehicle, (3) the weather condition (Sunny, Afternoon, Rainy, Night), and (4) the list of allowed vehicle type classes. The model is instructed to identify the most prominent vehicle visible in the image, use the waterline position relative to visible wheel and chassis features as the primary depth cue, and return a JSON object with flood depth in centimeters at 1-cm resolution.

The output format is strictly constrained to a single JSON line: `{"flood_depth_cm": <int>}`. During training, the label is always a valid JSON object with an integer depth in the range [0, 40]. A prompt ablation study on a 1,000-sample validation set showed that the schema-first prompt,

which includes explicit JSON schema guidance, achieved the lowest MAE (4.28 cm) for llama 3.2 base model, reducing error by 14.5% compared to a minimal prompt. Therefore, the schema-first design was adopted for all subsequent training.

```
SYSTEM:
You are a flood depth estimation assistant. Analyse the image and return ONLY
valid JSON:
{"flood_depth_cm": <int>}
Use 1-cm resolution. Output nothing else.

USER:
Estimate the flood depth for the most prominent vehicle in this image.
Vehicle metadata - TireHeight_cm: {tire_h} | GroundClearance_cm: {gc}
Weather: {weather} | AllowedVehicleTypes: {types}
Focus on the waterline relative to wheel and chassis features.

ASSISTANT:
{"flood_depth_cm": 15}
```

Figure 6. The example of Fine-Tuning Prompt Template.

### QLoRA Fine-Tuning Strategy

To train the model on a single RTX 4090 GPU (24 GB), a two-phase strategy was used (Figure 7). Phase 1 performs supervised fine-tuning on the single-vehicle dataset for three epochs to learn the mapping between visual flood cues and depth labels. Phase 2 progressively trains the model on several 30,000 sample chunks from the mixed-vehicle dataset, starting from the previous checkpoint. This approach improves memory efficiency while exposing the model to more complex scenes and results in stable training without catastrophic forgetting. The LLaMA 3.2-11B Vision Instruct model was first fine-tuned on 340,416 single-vehicle synthetic images and the training configuration is shown in Table 9.

To incorporate more complex scenes, the mixed-vehicle dataset (269,468 images) was introduced through a cumulative fine-tuning strategy. The data were divided into several sequential chunks (30,000 samples each), and the model was iteratively fine-tuned on each chunk for one epoch using a reduced learning rate of  $5 \times 10^{-5}$ . Training loss decreased monotonically from 0.0767 to 0.000971, indicating stable convergence without catastrophic forgetting. The final deployment checkpoint named Retune9 and evaluated on the same test set used in Phase 1 assessment. The improvement is dramatic: MAE falls from 5.65 cm to 0.40 cm — a 92.9% reduction — and RMSE drops from 7.38 cm to 1.97 cm. Exact-match accuracy (tolerance = 0) rises from 23.23% to 94.92%, and within-5 cm accuracy reaches 97.59%. The within-10 cm accuracy is 99.67%, indicating that fewer than 0.35% of predictions deviate by more than 10 cm.

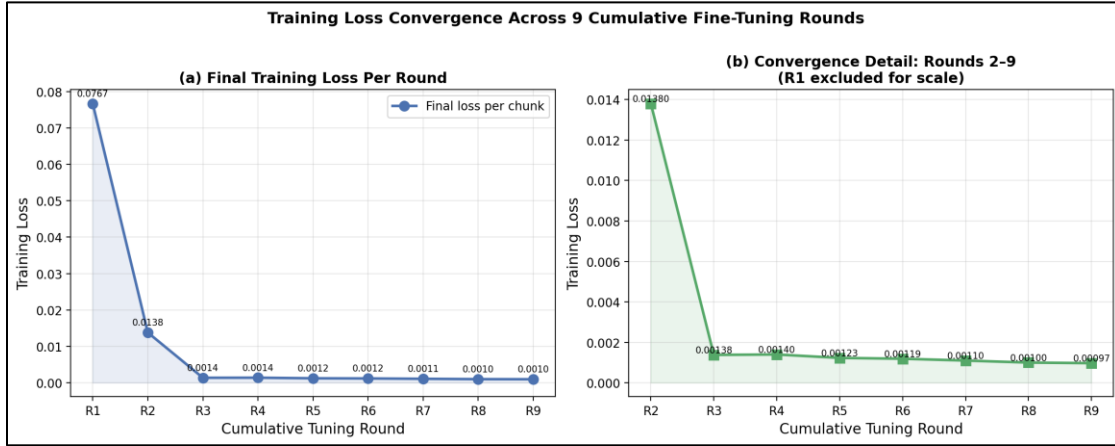
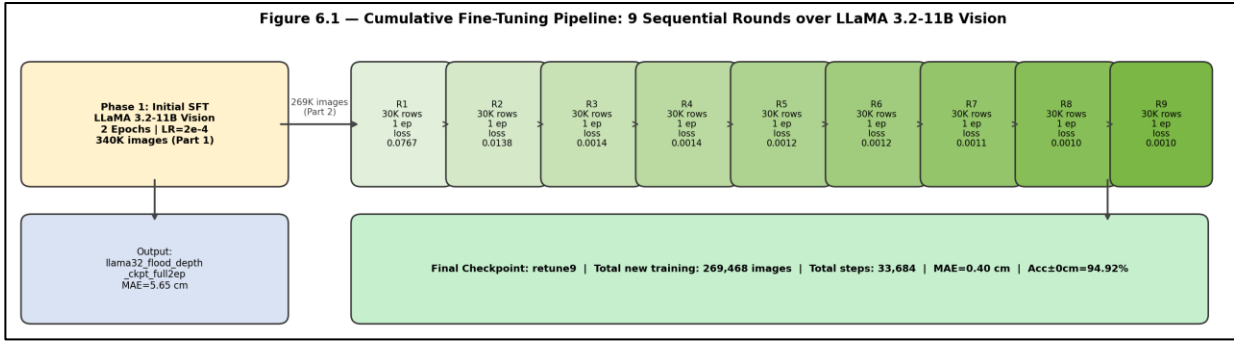


Figure 7. The training loss convergence across 9 cumulative re-tuning rounds. Loss drops from 0.0767 (round 1) to 0.000971 (round 9), indicating stable convergence without divergence or catastrophic forgetting.

Table 9. The training configuration and performance of the LLaMA-3.2 Vision flood depth estimation model.

Category	Parameter / Metric	Value
<b>Phase 1: Training Configuration</b>	Training data	340,416 samples (single vehicle)
	Dataset split	50/50 scene-level train/test
	Epochs	3
	Learning rate	$2 \times 10^{-4}$
	LR schedule	Cosine annealing (10 warm-up steps)
	Per-device batch size	2
	Gradient accumulation	4
	Effective batch size	8
	Steps per epoch	3,750
	Optimizer	AdamW (Paged)
	Hardware	NVIDIA RTX 4090 (24 GB VRAM)
Training duration	10.3 hours	
Output checkpoint	llama32_flood_depth_ckpt_full2ep	
<b>Phase 1: Evaluation (Test Set)</b>	MAE (cm)	5.65
	RMSE (cm)	7.38
	Accuracy ±0 cm	23.23%
	Accuracy ±5 cm	75.42%
<b>Phase 2: Cumulative Fine-Tuning</b>	Number of rounds	9
	Chunk size	30,000 samples per round
	Learning rate	$5 \times 10^{-5}$
	Epochs per round	3
	Training loss (Round 1 → 9)	0.0767 → 0.000971

Final Model Performance	MAE (cm)	0.40
	RMSE (cm)	1.97
	R <sup>2</sup> Score	0.9512
	Accuracy ±0 cm	94.92%
	Accuracy ±5 cm	97.59%
	Accuracy ±10 cm	99.67%

## Overall Performance Evaluation

### Depth-Stratified Performance Analysis

To understand how performance varies across the operational depth range, the test set is stratified into four categories: Low (1–10 cm), Medium (11–20 cm), High (21–30 cm), and Very High (31–40 cm). Table 10 presents depth-stratified MAE and within-5 cm accuracy for the retune9 model. Accuracy is uniformly high (>96.8%) across the Low, Medium, and High categories. A modest decline is observed in the Very High category, where MAE rises to 0.97 cm and within 5 cm accuracy falls to 93.7%. This behavior is consistent with the fact that at depths above 30 cm, the water surface rises above the wheel arch for many vehicle types, reducing the discriminative power of wheel-waterline cues. Figure 8 shows the accuracy heatmap showing the percentage of predictions within each tolerance threshold (0, 5, 10 cm) stratified by depth category. The Very High (31–40 cm) category shows the largest residual errors, suggesting reduced wheel-visible cues at extreme.

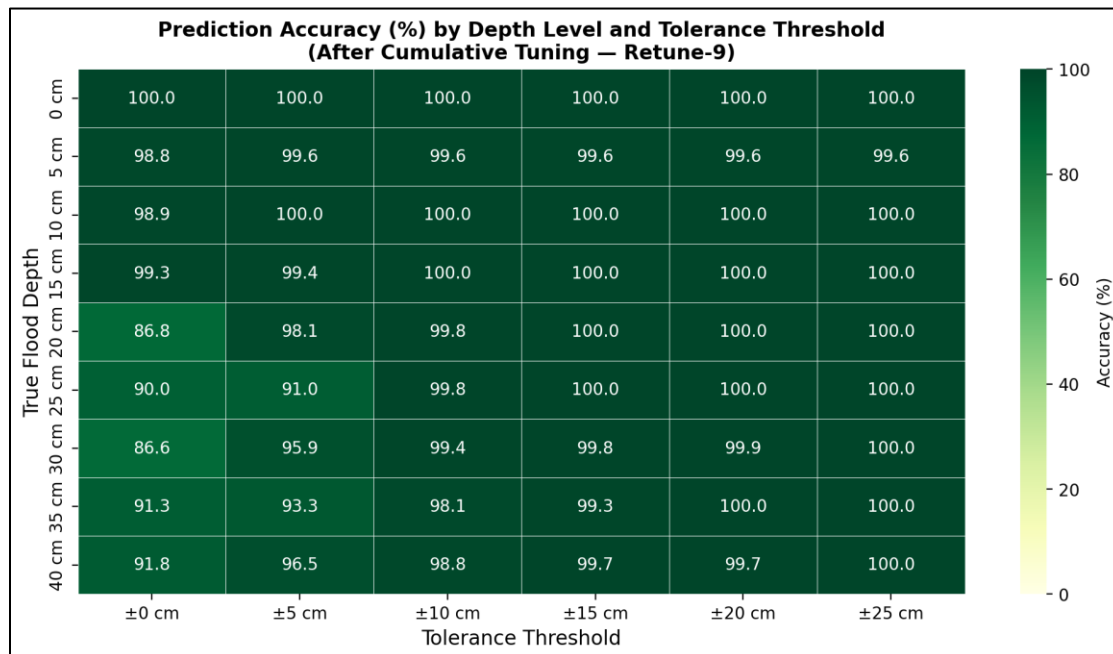


Figure 8. The accuracy heatmap by depth level and tolerance threshold.

Table 10. The depth-stratified performance — Retune 9.

Depth Category	Range (cm)	MAE (cm)	Acc $\pm 5$ cm
Low	1–10	0.18	99.1%
Medium	11–20	0.31	98.2%
High	21–30	0.54	96.8%
Very High	31–40	0.97	93.7%
Overall	1–40	0.40	97.59%

### Directional Bias Analysis

Beyond scalar error metrics, understanding the directional bias of predictions is critical for safety-informed deployment. An under-prediction (predicted depth < true depth) may lead operators to underestimate flood severity, whereas over-prediction causes unnecessary vehicle restrictions. Figure 9 presents the over/under prediction breakdown by depth category. In the Low depth category, the model is nearly symmetric (slight over-prediction tendency of  $\sim 1.2\%$ ). In the Medium and High categories, the model exhibits a mild under-prediction bias, particularly for depths above 20 cm, where the signed mean error is negative (predicted < actual). In the Very High category, this under-prediction bias is most pronounced, with approximately 12% more under-predictions than over-predictions. This systematic pattern suggests the model anchors on wheel features that become partially submerged at high flood depths, causing it to conservatively estimate lower depths when visual confirmation cues are limited.

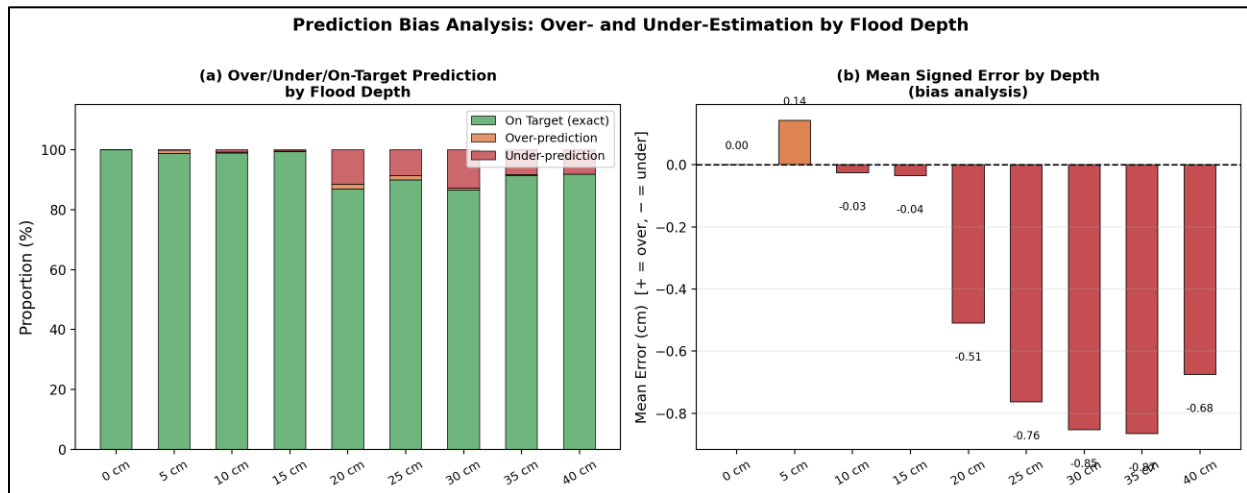


Figure 9. The over/under prediction analysis by depth category (retune9).

## MECHANISTIC INTERPRETABILITY OF THE FINE-TUNED MODEL

This work investigates *how* QLoRA fine-tuning transforms Llama 3.2 11B Vision from a general-purpose vision-language model (VLM) into a precise flood depth estimator. Rather than treating

the fine-tuned model as a black box, we apply mechanistic interpretability to expose the internal circuit changes responsible for task acquisition. The central hypothesis is that QLoRA selectively restructures a small subset of the eight cross-attention layers, the only conduit through which visual information enters the language decoder in this architecture and that identifying those layers enables principled, parameter-efficient fine-tuning. We pursue three concrete objectives: (1) Identify which cross-attention layers encode depth information after fine-tuning and which do not, (2) establish the causal role of each layer through perturbation experiments and, 3) translate those findings into selective fine-tuning architectures that preserve task performance with a fraction of the trainable parameters.

### **Phase 1: Identifying Where Flood Knowledge Resides**

The adapter weight analysis reveals three clear findings (Figure 10). First, adaptation is concentrated in the five cross-attention layers (18, 23, 28, 33, 38), which are precisely the layers responsible for fusing visual and language representations — confirming that the model learns flood depth by re-weighting how it attends to visual features rather than by modifying its general language reasoning (Table 11). The weight updates which are uneven across layers, with layers 23, 18, 28, 33, and 38 showing the largest changes (150–206), about 2.5–3× higher than the average, indicating that flood-depth reasoning concentrates in mid-to-upper transformer layers. These layers correspond to cross-attention blocks, where the largest updates occur in `q_proj` and `o_proj`, suggesting adaptation in how visual features are queried and projected. Second, MLP gate projections accumulate the highest total change, indicating that the feed-forward memory of the model is being updated to store flood-depth-specific visual-to-numerical mappings. The MLP projections dominate the updates, particularly `gate_proj` (864), `down_proj` (710), and `up_proj` (691), followed by `q_proj` (514) and `o_proj` (465), while `v_proj` (201) changes least, indicating that feed-forward layers primarily encode the mapping between visual cues (e.g., waterline height and wheel occlusion) and numerical flood depth. Third, the near-rank-1 singular value structure of several high-change modules suggests that the most critical adaptations are low-dimensional: the model learns a small number of dominant directions in weight space rather than diffuse, high-dimensional updates, which is consistent with the efficient convergence observed during cumulative tuning (training loss reaching 0.000971 after nine rounds). Several modules show rank-1 dominated singular value spectra, indicating adaptation along a few dominant weight directions, while layer 23 `cross_attn.o_proj` exhibits more distributed changes, and the near-linear relation

between Frobenius and spectral norms confirms that modules with larger updates also contain stronger dominant singular values, consistent with efficient convergence (Figure 11).

Table 11. The change of different layers inside the Fine-Tuned model.

Module Type	Total $\ \Delta W\ _F$	Role
gate_proj	863.97	MLP gating — highest change
down_proj	710.36	MLP projection (output)
up_proj	691.26	MLP projection (intermediate)
q_proj	513.69	Attention query — driven by cross-attn layers
o_proj	464.98	Attention output
k_proj	270.85	Attention key
v_proj	201.50	Attention value — least changed

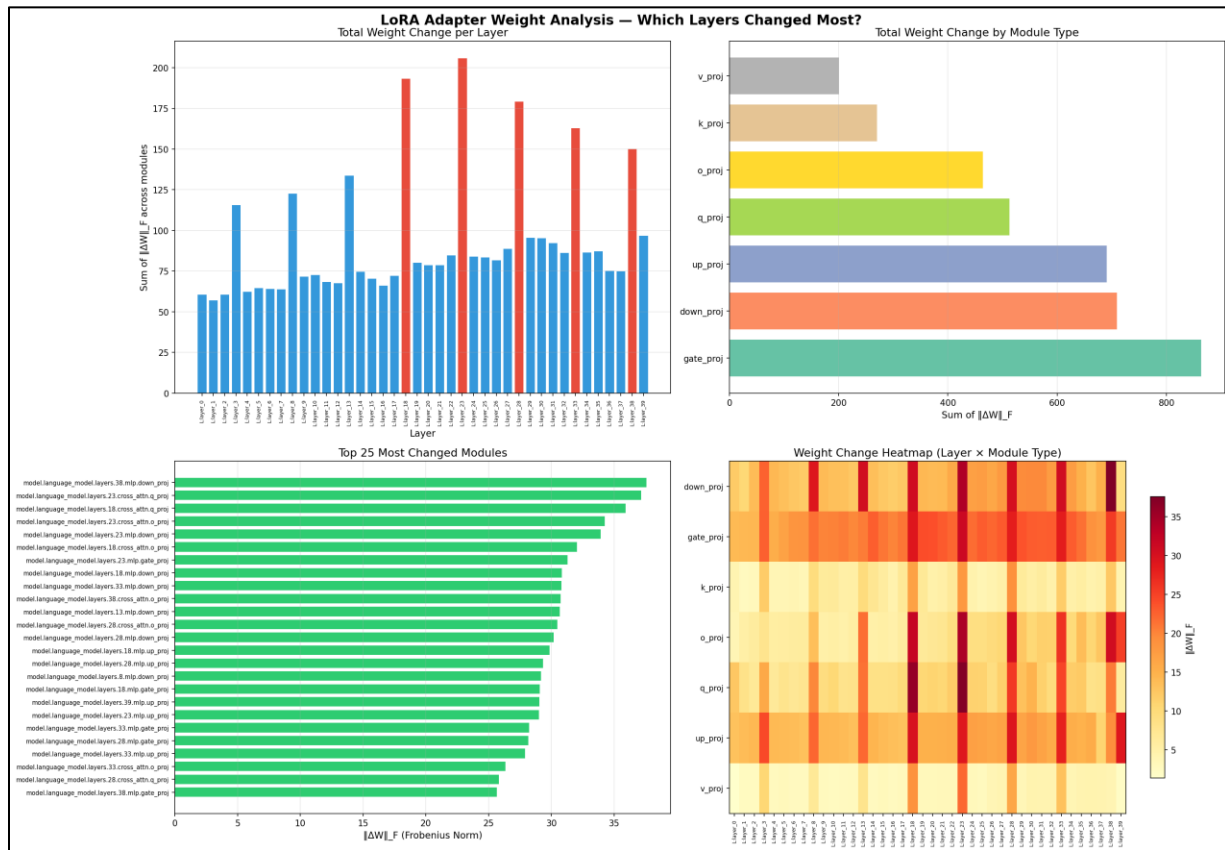


Figure 10. The LoRA adapter weight analysis. Top-left: total weight change ( $\|\Delta W\|_F$ ) per layer — five cross-attention layers (18, 23, 28, 33, 38) dominate. Top-right: cumulative change by module type, showing MLP gate/down/up projections absorb the most adaptation energy. Bottom-left: top 25 individual modules ranked by  $\|\Delta W\|_F$ . Bottom-right: heatmap of change intensity (layer  $\times$  module type), highlighting the cross-attention layer hotspots.

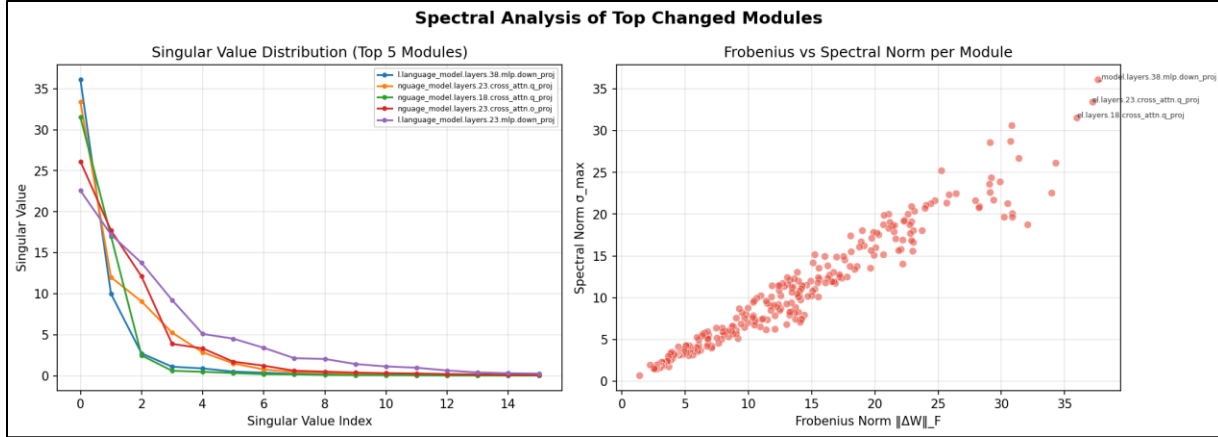


Figure 11. The Spectral analysis of the top changed modules. Left: singular value decay for the five most-changed modules. Right: Frobenius norm vs. spectral norm ( $\sigma_{\max}$ ) across all 280 modules — the linear relationship confirms consistent rank structure throughout the adapter.

## Phase 2: Prompt Sensitivity and Attention Behavior

A fundamental question in deploying vision-language models for structured prediction tasks is whether the choice of input prompt materially affects inference quality. This section evaluates how different prompt formulations affect prediction accuracy and spatial attention in foundational model (LLaMA 3.2-11B Vision) for flood depth estimation. Seven prompt strategies are tested on 4,971 synthetic images across four weather conditions (34,797 evaluations, with cross-attention maps used to visualize where the model focuses during prediction). The results demonstrate that prompt design is a critical factor: transitioning from an unguided prompt to a schema-anchored formulation reduces the mean absolute error by more than  $2.7\times$  and produces qualitative changes in prediction behavior, not merely quantitative improvements. Attention patterns remain spatially similar across prompts, indicating that accuracy improvements arise from better output structure rather than changes in visual focus.

### *Prompt-Driven Attention Visualization: Does Prompt Choice Alter Model Focus?*

Cross-attention maps from the eight multimodal layers (3, 8, 13, 18, 23, 28, 33, 38) were averaged across heads and overlaid on images to examine prompt-induced attention shifts. The spatial focus remained largely unchanged across all seven prompt strategies, consistently targeting the vehicle body, wheel arches, and waterline—while prediction accuracy varied substantially (Figure 12). Statistical analysis shows negligible correlation between attention patterns and error ( $r=0.032$ ,  $p<0.001$ ), indicating that prompt sensitivity primarily affects language-side reasoning and output structure rather than visual attention.

Seven prompt strategies with varying guidance levels were evaluated to assess their impact on flood depth prediction. The detailed prompt, which enforces a strict JSON schema with vehicle metadata, achieved the best performance (Table 12). In contrast, chain-of-thought, structured, and reference prompts produced near-constant predictions, leading to high errors (~38–39 cm MAE). The multi\_cue and simple prompts showed moderate performance but were unstable across conditions, while the vague prompt produced no valid outputs. Overall, the results indicate that explicit output schemas and structured guidance are essential for reliable depth estimation with vision–language models.

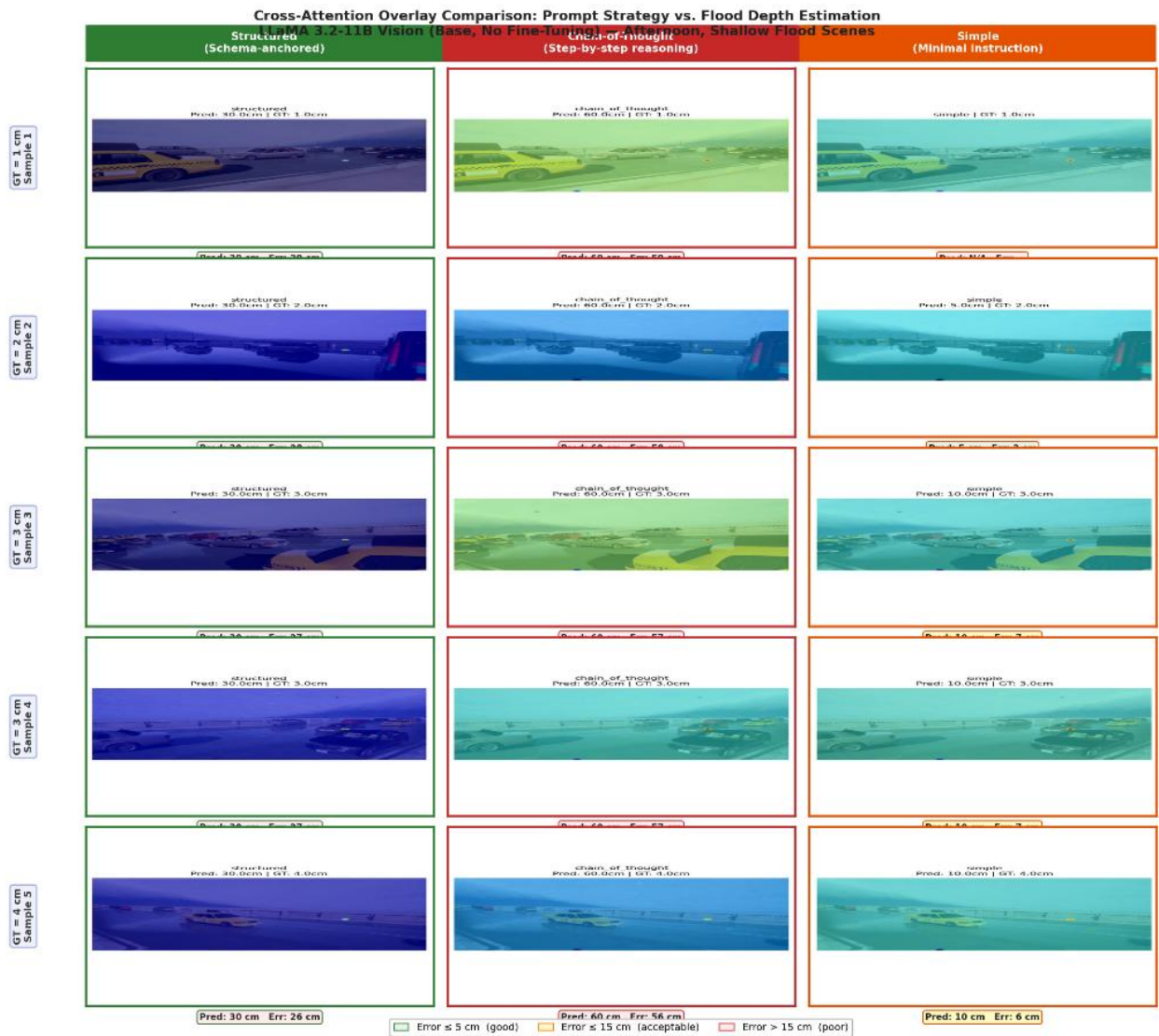


Figure 12. The cross-attention overlay comparison: prompt strategy vs flood depth estimation.

Table 12. The seven prompt strategies error analysis.

Prompt	MAE (cm)	Std (cm)	Median Error	Within 5 cm	Within 10 cm	Pred. Rate
Detailed	14.07	8.57	14.0	21.0%	37.1%	100%
Multi cue	23.72	31.56	13.0	20.0%	41.0%	100%
CoT	38.43	12.89	39.0	1.4%	2.1%	100%
Structured	38.46	12.04	39.0	0.5%	0.7%	100%
Reference	39.40	11.70	39.0	0.0%	0.1%	100%
Simple	45.20	51.27	20.0	19.8%	32.1%	88.2%
Vague	N/A	N/A	N/A	—	—	0%

### Attention Overlay Analysis on Cross-Attention Layers

Table 13 presents cross-attention statistics extracted across all 34,797 forward passes. Sparsity (range 0–1) measures attention concentration; a value near 1 indicates the model allocates attention selectively to a small number of image patches. Entropy standard deviation captures how stable the attention pattern is across different samples under the same prompt. The detailed prompt yields the most stable and focused attention, consistently directing attention to the vehicle and waterline region. Chain of Thought also shows moderate focus with less stability. In contrast, prompts with large entropy variance (e.g., Multi\_cue, structured, vague) exhibit unstable attention spikes and higher prediction errors. The detailed prompt also maintains consistent accuracy across weather conditions, indicating that schema-guided prompts provide robust and reliable model behavior.

Table 13. The cross-attention behavior across prompt strategies on Llama 3.2 11B based model.

Prompt	Sparsity	Entropy (mean)	Entropy Std	Focus (mean)	Interpretation
Detailed	0.961	6.15	$\pm 1.22$	5.22	Stable, focused highest reliability
Chain of thought	0.920	6.94	$\pm 12.9$	8.35	Moderate focus, stable
Reference	0.914	7.72	$\pm 20.9$	8.97	Moderate focus, unstable
Multi cue	0.858	-10.24	$\pm 765.9$	36.10	Frequent attention spikes
Structured	0.818	-20.90	$\pm 2,062$	48.57	Erratic outlier-dominated
Simple	0.665	-14.93	$\pm 911$	93.45	Diffuse and unstable
Vague	0.651	-345.07	$\pm 18,938$	316.78	Completely chaotic

### Phase 3: Layer Ablation and Statistical Analysis

In standard multimodal VLM inference, attention is typically aggregated across all cross-attention layers (Abnar & Zuidema, 2020). However, different layers may contribute unequally depending on the visual task (Chefer et al., 2021). Flood depth estimation is a fine-grained regression problem that relies on subtle geometric cues such as waterline position, tire submersion, and wheel arch occlusion rather than broad semantic features. This raises an important interpretability question: which cross-attention layers in LLaMA 3.2-11B Vision carry the most depth-related information,

and whether the optimal layer selection varies with scene complexity, flood depth, or prompt design. Identifying these layers not only provides practical guidance for inference but also offers insight into the model’s internal mechanism for visual depth reasoning.

The study systematically evaluates all non-empty subsets of the eight multimodal cross-attention layers (L3, L8, L13, L18, L23, L28, L33, L38) and selects, for each experimental condition, the subset that minimizes MAE. Two datasets are analyzed: a single-vehicle dataset covering three vehicle classes—Big (bus, trailer, van), Medium (SUV, minivan, truck), and Sedan—across four weather conditions, three prompt strategies (Detailed, Chain-of-Thought (CoT), and Simple), and eight flood depths (5–40 cm), yielding 287 configurations; and a multi-vehicle dataset with 96 configurations. The baseline uses the full-layer average (all eight layers aggregated), representing the standard inference approach. The Detailed and CoT prompts were selected based on their stronger inference performance observed in Phase 2, while the Simple prompt was included for comparison.

#### *Principal Findings from Ablation Study*

The most immediately actionable finding is that using all eight cross-attention layers simultaneously is suboptimal. Optimal configurations use on average only 3.1 layers (out of 8), reducing the mean MAE from 12.46 cm (full-layer baseline) to 4.76 cm across all 383 configurations — a 59% reduction. Furthermore, 52 of 287 single-vehicle configurations and 12 of 96 multi-vehicle configurations achieve perfect predictions (MAE = 0.00 cm) with the optimal subset, a result impossible under the standard full-layer aggregation. This demonstrates that redundant or noisy layers actively suppress the signal carried by the most informative cross-attention heads.

A four-way ANOVA (prompt × car × weather × depth) on single-vehicle configurations explains 79.7% of variance ( $R^2 = 0.797$ ). Flood depth alone accounts for the largest share ( $\eta^2 = 0.38$ , large effect,  $p < 10^{-43}$ ), with MAE rising monotonically as depth increases. Vehicle type and weather are statistically non-significant ( $p = 0.13$  and  $p = 0.11$  respectively), confirming that the model’s depth estimation pathway is largely invariant to these factors. The critical moderating effect is the prompt × depth interaction ( $\eta^2 = 0.31$ , large,  $p < 10^{-33}$ ): the relative accuracy of each prompt strategy inverts as a function of depth, with a crossover occurring around 27–30 cm. Below

this threshold, Simple prompts are superior which entails that simple prompt works better for task specific layers rather full layer aggregation; above it, Chain-of-Thought takes the lead.

This crossover has a mechanistic interpretation (Figure 13): shallow floods present strong, localized visual cues (wheel contact zone, clear waterline) that are captured by direct one-shot attention. A simple prompt exploits this by allowing the model to directly pattern-match depth indicators without over-constraining the reasoning path. Deeper floods produce partial occlusion, ambiguous gradients, and multiple competing depth cues; here, the step-by-step structure of chain-of-thought directs the model to reason through each cue sequentially rather than committing to a single-step comparison. Critically, CoT achieves zero perfect predictions in single-vehicle scenes, whereas Simple and Detailed together account for all 52 perfect predictions — confirming that CoT’s reasoning process, while robust, introduces a systematic positive bias that prevents exact estimation even when all cues are unambiguous.

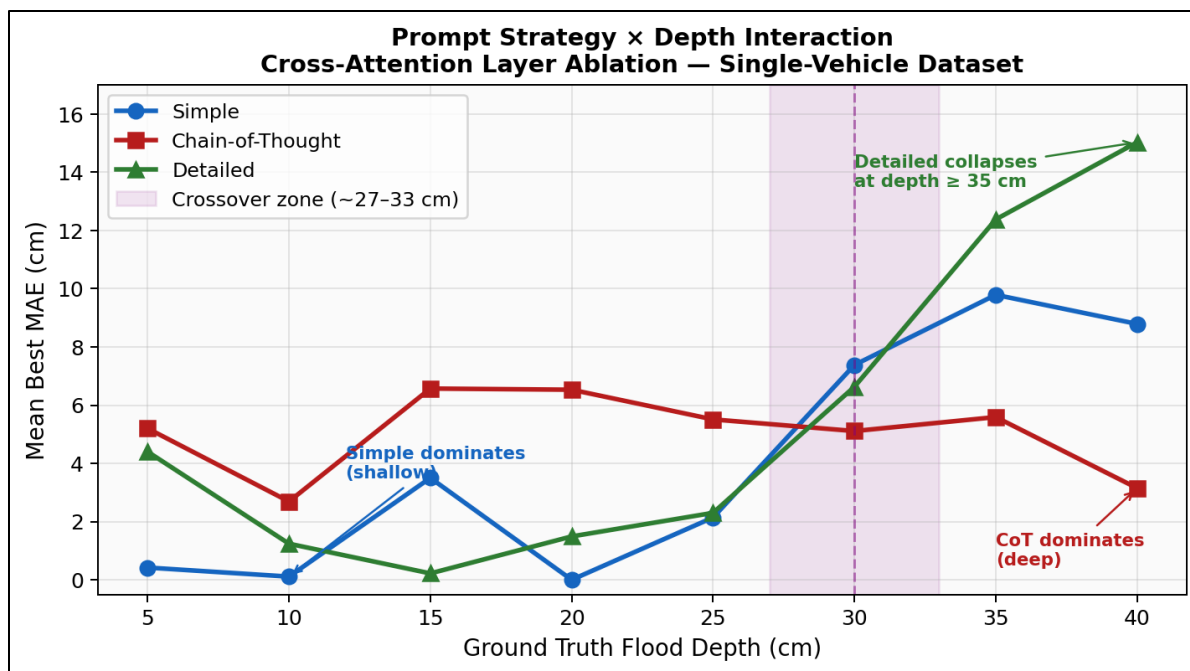


Figure 13. The Prompt strategy  $\times$  flood depth interaction.

The optimal layer set is not fixed across depth ranges but follows a consistent pattern (Figure 14). At shallow depths (5–10 cm), early layers L3 (66%) and L28 (69%) dominate, suggesting that low-level edge and texture features suffice when the waterline is close to the image baseline and unambiguous. At moderate depths (15–20 cm), the layer set collapses to a single dominant integrator: in multi-vehicle scenes, L38 alone achieves four perfect predictions at 15 cm

(Detailed prompt), indicating that the final cross-modal integration layer carries all necessary depth information once moderate flood features are present. At deeper scenes (35–40 cm), a broad coalition of mid-to-late layers (L8, L18, L23, L33) is required, reflecting the need for distributed visual reasoning across multiple occlusion levels.

L13 is consistently excluded from optimal configurations, appearing in only 23.0% (single vehicle) and 20.8% (multi-vehicle) cases, with the highest chi-square contribution in both datasets. This suggests L13 operates at an intermediate feature-integration stage that introduces noise rather than useful depth signals; therefore, excluding L13 is recommended across conditions. Although overall MAE is similar between datasets (Mann–Whitney  $p = 0.999$ ), multi-vehicle scenes rely more on the final cross-attention layer (L38), which appears in 62.5% of optimal configurations (vs. 43.2% in single-vehicle scenes). This indicates that complex scenes require stronger high-level cross-modal integration, making L38 particularly important for multi-vehicle flood analysis.

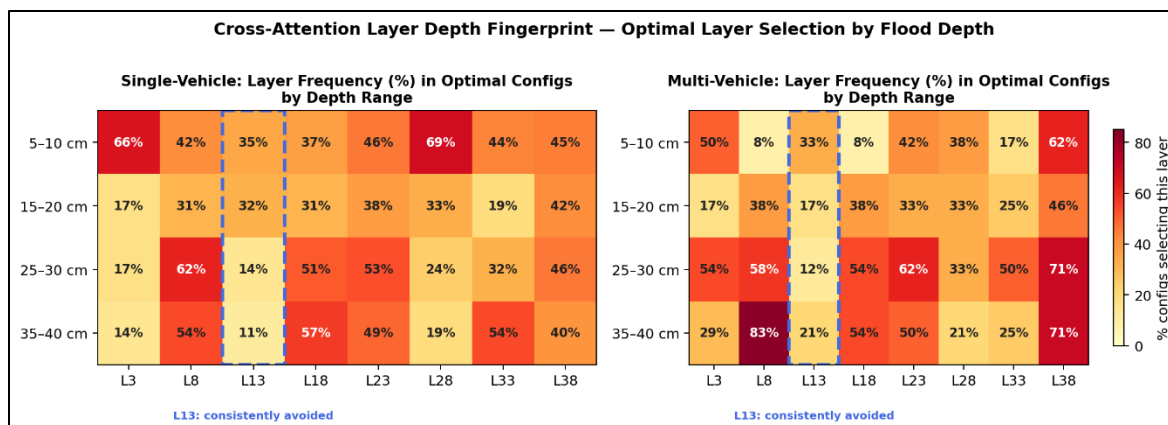


Figure 14. The Cross-attention layer frequency (%) in optimal configurations, stratified by flood depth range.

#### Phase 4: Four-Method Mechanistic Dissection

For this experiment, we compare the LLaMA 3.2 11B Vision base model with the retune9 fine-tuned model, with both models loaded in fp16 precision. A set of mechanistic interpretability analyses is applied to examine the differences between the base and fine-tuned models and to identify which layers contribute most strongly to task-specific learning. The experiments use a synthetic flood imagery dataset of 12,800 images, consisting of 9,600 single-vehicle images (3 vehicle types  $\times$  4 weather conditions  $\times$  8 depth levels  $\times$  100 images per cell) and 3,200 multi-vehicle images (4 weather conditions  $\times$  8 depth levels  $\times$  100 images). Flood depth labels range

from 5–40 cm in 5 cm increments. For interpretability analysis, a subset of 480 images (5 per cell) is used, while fine-tuning experiments use 8,640 images for training and 960 for evaluation.

### *Linear Probing for Depth Information Decoding*

Table 14 reports the linear probing results for each cross-attention layer of the base and fine-tuned models. Linear probing evaluates whether information relevant to a target variable—in this case flood depth—is linearly decodable from intermediate hidden representations by training a simple linear regressor on frozen model activations. If a layer contains usable task information, the probe should achieve positive predictive performance ( $R^2 > 0$ ); negative values indicate that the representation does not encode the target signal beyond a trivial baseline. Linear probes are widely used in representation analysis because they provide a minimal and interpretable method for measuring how much task-relevant information is present in different layers of neural network without altering the model itself (Alain & Bengio, 2018; Belinkov, 2022).

As shown in Table 14, the base model exhibits  $R^2 < 0$  at all layers, indicating that flood depth is not linearly decodable from its hidden states. After QLoRA fine-tuning, a sharp phase transition occurs at layer L23, where  $R^2$  increases from  $-0.355$  at L18 to  $+0.513$  at L23 ( $\Delta R^2 = +0.772$ ). The subsequent layers (L23–L38) maintain strong linear decidability ( $R^2 \approx 0.51$ – $0.56$ ) and reduce probe MAE from approximately 9 cm to 4.5–5.0 cm, demonstrating that depth-related information becomes explicitly encoded in the upper cross-attention layers. In contrast, layers L3–L18 remain at  $R^2 < 0$  even after fine-tuning, suggesting that earlier layers primarily process visual features without directly representing depth information.

*Table 14. The linear probe results at each cross-attention layer.*

Layer	Base $R^2$	FT $R^2$	$\Delta R^2$	Base MAE (cm)	FT MAE (cm)	$\Delta$ MAE (cm)
L3	-0.301	-0.317	-0.016	9.81	9.86	+0.05
L8	-0.322	-0.270	+0.052	9.40	9.41	+0.01
L13	-0.333	-0.324	+0.009	9.22	9.54	+0.32
L18	-0.305	-0.355	-0.050	8.95	9.68	+0.73
L23	-0.259	+0.513	+0.772	8.77	5.02	-3.75
L28	-0.200	+0.559	+0.759	8.37	4.69	-3.68
L33	-0.232	+0.553	+0.785	8.34	4.58	-3.76
L38	-0.305	+0.551	+0.855	8.51	4.52	-3.99

*Note:  $\Delta R^2 = FT R^2 - Base R^2$ .  $\Delta$ MAE = FT probe MAE – Base probe MAE (negative = improvement). Orange part indicates improvement in fine-tuning model layers.*

## Logit Lens: Tracing Visual-to-Language Alignment

Table 15 shows the dominant token categories decoded from each cross-attention layer using the logit lens technique. Logit lens is an interpretability method that projects intermediate hidden states directly into the model’s vocabulary space using the final output (unembedding) matrix, allowing researchers to inspect which tokens a layer is implicitly representing before the final decoding step. This approach helps trace how internal representations evolve toward meaningful language outputs across layers (Neo et al., 2025). It is particularly suitable here because the task involves predicting structured numerical outputs from visual inputs, and logit lens reveals whether intermediate representations begin to encode task-relevant vocabulary—such as flood-related terms or numerical tokens—before the final generation stage.

As shown in Table 15, both the base and fine-tuned models produce largely incoherent subword tokens at layers L3–L23, indicating that early representations do not yet correspond to meaningful language. Semantically interpretable tokens begin to appear only in the upper layers (L28–L38). The base model gradually converges to general scene-description vocabulary (e.g., “vehicles,” “flooded,” “cars”), whereas the fine-tuned model shows numeric tokens at L33 and output-format tokens at L38 consistent with its JSON response structure. This pattern supports the linear probing results, confirming that task-relevant depth information becomes accessible primarily in the final cross-attention layers.

Table 15. The logit lens token categories per layer.

Layer	Base — Dominant Tokens	FT — Dominant Tokens	Semantic Stage
L3	Foreign subwords: ‘gc’, ‘ichert’, ‘gezocht’	Code fragments : ‘#ab’, ‘#ac’, ‘)frame’	Incoherent
L8	Mixed subwords: ‘oví’, ‘Sharper’, ‘acr’	Code tokens : ‘#ab’, ‘#af’, ‘/***’	Incoherent
L13	Subwords: ‘oví’, ‘)test’, ‘ernote’	Code tokens : ‘#ab’, ‘#af’, ‘-*_’	Incoherent
L18	Code artefacts: ‘#ab’, ‘-wsj’, ‘akra’	Code artefacts: ‘#af’, ‘-wsj’, ‘/***’	Incoherent
L23	Code artefacts : ‘/***’, ‘#ab’, ‘)frame’	Code artefacts: ‘#af’, ‘#ab’, ‘/***’	Incoherent
L28	Mixed: ‘/***’, ‘flooded’ (11x), ‘cars’ (9x)	Fragments: ‘PackageManager’, ‘units’, ‘NEWS’	Scene words emerging (base)
L33	‘vehicles’ (27x), ‘image’ (19x), ‘flooded’ (9x)	Symbols + numerics: ‘59’ (9x), ‘426’ (3x)	Scene description (base); numeric (FT)
L38	‘image’ (20x), ‘vehicles’ (17x), ‘flood’ (13x)	Function words: ‘the’, ‘depth’ (9x), ‘assistant’, ‘23’	Scene description (base); output format (FT)

### Centered Kernel Alignment (CKA): Representational Divergence

Table 16 reports the similarity between base and fine-tuned representations using CKA. CKA is a representation-similarity metric that measures how similar two sets of neural activations are across models or training stages, with values close to 1 indicating nearly identical representations and lower values indicating stronger divergence (Kornblith et al., 2019). CKA is widely used in deep learning interpretability because it is invariant to orthogonal transformations and scaling, making it well suited for comparing hidden representations across layers and model variants. In this study, CKA is used to quantify how fine-tuning alters the internal representations of the LLaMA 3.2 Vision model at each decoder layer.

As shown in Table 16, the largest representational divergence occurs around layers L13–L22, with the global minimum at L17 (CKA = 0.395). Among the cross-attention layers, L13 diverges the most (CKA = 0.457), while L8 changes the least (CKA = 0.852). Importantly, these highly altered layers do not correspond to those that encode flood-depth information identified by linear probing (L23–L38). This mismatch indicates that early layers undergo substantial representational restructuring without directly contributing to depth encoding, suggesting a two-stage adaptation process in which early layers reorganize features while later layers perform task-specific depth computation.

Table 16. The per-layer CKA (Base to Fine-Tuned) across all 40 decoder layers.

Layers	CKA	Layers	CKA	Layers	CKA	Layers	CKA
L0	NaN	L10	0.838	L20	0.501	L30	0.725
L1	NaN	L11	0.825	L21	0.495	L31	0.724
L2	NaN	L12	0.823	L22	0.481	L32	0.709
L3 *	0.685	L13 *	0.457	L23 *	0.679	L33 *	0.698
L4	0.644	L14	0.456	L24	0.673	L34	0.701
L5	0.658	L15	0.441	L25	0.677	L35	0.711
L6	0.672	L16	0.424	L26	0.656	L36	0.726
L7	0.650	L17	0.395	L27	0.639	L37	0.728
L8 *	0.852	L18 *	0.506	L28 *	0.749	L38 *	0.775
L9	0.855	L19	0.499	L29	0.746	L39	0.743

Notes: (\*) means cross-attention layers. CKA = 1 = identical; lower = more diverged. Layers 0–2 returned NaN.

### Cross-Attention Maps and Entropy Comparison

Table 17 reports the spatial characteristics of cross-attention using attention entropy and prompt sensitivity metrics. Shannon entropy measures the dispersion of attention across image patches: lower entropy indicates more spatially focused attention, while higher entropy reflects diffuse attention over many regions (Shannon, 1948). As shown in Table 17, the fine-tuned model exhibits

more focused attention overall (mean entropy 7.152 vs. 7.264 in the base model). The largest entropy reduction occurs at L13 ( $\Delta H = -0.304$ ), which coincides with the layer showing the largest representational divergence in the CKA analysis. However, despite this sharper spatial focus, L13 still does not encode flood depth information ( $R^2 = -0.324$  in the probing analysis).

Table 17. The attention entropy and prompt sensitivity per layer.

Layer	Base Entropy	FT Entropy	$\Delta$ Entropy
L3	7.385	7.424	+0.039
L8	7.357	7.241	-0.116
L13	7.311	7.007	-0.304
L18	7.383	7.136	-0.248
L23	7.402	7.273	-0.129
L28	7.179	6.979	-0.201
L33	6.927	6.900	-0.027
L38	7.168	7.256	+0.088

### Phase 5: Synthesis and Composite Layer Ranking

Table 18 consolidates the evidence from all methods into normalized importance scores. Each metric is min-max normalized to  $[0, 1]$  across the eight cross-attention layers, then averaged into a composite score. A higher composite score indicates a layer is important by more lines of evidence simultaneously. The composite evidence reveals a two-stage adaptation mechanism across the cross-attention layers. Early-to-mid layers (L13–L18) primarily perform representational restructuring, showing substantial parameter updates, representational divergence, and increased spatial selectivity, yet linear probing indicates that depth information remains largely undecodable at this stage. Functional depth encoding emerges only at L23, which achieves the highest composite importance score (0.768) and marks the point where restructured visual features are first converted into an explicit numerical depth estimate. Downstream layers (L28–L38) maintain strong probe performance and contribute to integrating visual cues with linguistic representations to stabilize the final prediction, while early layers (L3–L8) exhibit low composite scores and minimal task-specific adaptation. Together, these results indicate that depth estimation in the fine-tuned model is primarily implemented in the mid-to-late cross-attention layers, with earlier layers serving preparatory representational roles rather than directly encoding the target variable.

Table 18. The ranking of cress attention layer using normalized composite score.

Layer	Ablation Freq.	$\ \Delta W\ $ Norm (XAttn)	Probe $\Delta R^2$	1 - CKA (divergence)	Entropy Focus ( $-\Delta H$ )	Composite Score	Rank
L3	0.316	0.000	0.037	0.422	0.125	0.180	8 <sup>th</sup>
L8	0.970	0.054	0.112	0.000	0.520	0.331	7 <sup>th</sup>
L13	0.000	0.220	0.066	1.000	1.000	0.457	6 <sup>th</sup>
L18	0.786	0.877	0.000	0.877	0.857	<b>0.679</b>	2 <sup>nd</sup>
L23	0.939	1.000	0.908	0.438	0.555	<b>0.768</b>	1 <sup>st</sup>
L28	0.490	0.692	0.893	0.261	0.738	<b>0.615</b>	3 <sup>rd</sup>
L33	0.500	0.454	0.922	0.390	0.293	<b>0.512</b>	4 <sup>th</sup>
L38	1.000	0.329	1.000	0.195	0.000	<b>0.505</b>	5 <sup>th</sup>

Note: L13 ranks unexpectedly due to its large CKA divergence and entropy drop, but its other effect is negative — it actively hurts model performance.

## FROM INTERPRETABILITY TO EFFICIENT TRAINING: SELECTIVE LAYER FINE-TUNING

### Tier Architecture Design from Composite Evidence

The composite evidence in Table 18 directly motivates the three-tier layer selection design. Table 19 shows how each tier was constructed and the explicit reasoning for including or excluding each layer. The anti-configuration deliberately inverts the evidence: L3 and L13, the two layers with the lowest composite scores and confirmed non-functional or harmful roles, are selected as the sole trainable layers. This tests whether the interpretability framework is predictive: if the rankings are meaningful, training only these layers should fail to acquire the task.

Table 19. The layer selection logic for each fine-tuning configuration.

Layer	Composite Score	Tier 1 (3 layers)	Tier 2 (5 layers)	Tier 3 (6 layers)	Anti-config	Rationale for decision
L3	0.163	×	×	×	✓	Lowest composite. Useful only at shallow depths; falling importance trend
L8	0.295	×	✓	✓	×	High ablation freq. (47.4%); visual feature extractor; adds coverage at 25–40 cm
L13	0.381	×	×	×	✓	Harmful: blocking improves FT by 0.55 cm. Excluded from all tiers
L18	0.597	✓	✓	✓	×	2nd highest composite; Stage 1 restructurer; 2nd largest $\Delta W$ ; prepares L23 input
L23	0.807	✓	✓	✓	×	Highest composite; phase transition layer
L28	0.514	×	×	✓	×	Strong probe $R^2$ ; dominant at 5–10 cm (69%); omitted from Tier 2 to test coverage
L33	0.434	×	✓	✓	×	Output refinement; rises to 54% importance at 35–40 cm; improves deep-water precision

L38	0.434	✓	✓	✓	✗	Critical for multi-vehicle (62.5%); strong probe R <sup>2</sup> ; final integration layer
-----	-------	---	---	---	---	---

### Trail Run on Selective Fine-Tuning

All four configurations were trained under identical conditions (QLoRA  $r = 16$ ,  $\alpha = 16$ , 3 epochs, effective batch size 16, 8640 images for training) and evaluated on 960 testing images mentioned in the Four-Method Mechanistic Dissection section. Table 9 reports overall performance and Table 10 provides the per-depth MAE breakdown. However, the targeted configurations derived from the mechanistic analysis demonstrate that strong performance can be achieved with substantially fewer trainable parameters. Tier 3 (L8, L18, L23, L28, L33, L38) and Tier 2 (L8, L18, L23, L33, L38) maintain competitive accuracy while reducing the number of trainable parameters by approximately 76–80%. Notably, this performance is achieved with a relatively small training set, indicating that the key task-specific adaptations are concentrated in these mid-to-late cross-attention layers identified in the mechanistic study. By contrast, the Tier 1 configuration (L18, L23, L38) shows a moderate drop in performance, and the anti-configuration (L3, L13), which targets layers identified as least informative, performs substantially worse. Given this trade-off between efficiency and accuracy, Tier 2 and Tier 3 provide the most practical configurations for the final fine-tuned model, capturing most of the performance gains while keeping the number of trainable parameters small.

Table 20. The selective fine-tuning performance across different configurations.

Configuration	Layers	Trainable Params	MAE (cm)	RMSE (cm)	R <sup>2</sup>	Acc@5cm (%)
Tier 3	L8,18,23,28,33,38	12.4M	3.526	6.164	0.711	81.0
Tier 2	L8,18,23,33,38	10.3M	3.969	6.587	0.696	77.4
Tier 1	L18,23,38	6.2M	4.411	7.244	0.600	75.2
Anti-config	L3,13	4.1M	6.073	9.217	0.353	65.6

Note: The training dataset is relatively small, consisting of 8,640 training images and 960 evaluation images.

### Layer Efficient Fine-Tuning (Tier 2 and Tier 3)

Layer Efficient Fine-tuning was implemented using 4-bit NF4 quantization of the frozen base weights, combined with the PEFT library for adapter management. Adapters were instantiated, enabling resumption of existing adapters while keeping all base weights frozen. Training used the SFTTrainer from the TRL library. The following hyperparameters were held constant across all training phases:

Table 21. The fixed training hyperparameters.

Hyperparameter	Value
Effective batch size	16 images (4 per device $\times$ 4 gradient accumulation steps)
Sequence length	2,048 tokens
Optimizer	AdamW, weight decay = 0.01
LR scheduler	Cosine annealing, warmup ratio = 0.03
LoRA rank / alpha	$r = 16, \alpha = 16$ (scaling = 1.0)
LoRA target modules	cross attn (Q,K,V,O), self attn (Q,K,V,O), MLP (gate, up, down)
Precision	float16 (adapters); NF4 4-bit (frozen base weights)
Output format	{“flood_depth_cm”: N} (N $\in$ $\mathbb{Z}$ , 1–40)
Prompt	Detailed Prompt S

### Progressive Curriculum Training (Tier 2 and Tier 3)

A core insight from the mechanistic analysis is that the model must first establish stable coarse depth representations before being asked to resolve fine-grained 1 cm distinctions. Asking the model to jump directly from general visual understanding to discriminating 32 cm from 33 cm would require the cross-attention circuits to simultaneously solve two distinct learning objectives: feature selection (which visual cues encode depth?) and metric resolution (how precisely can those cues be measured?). We therefore we again design two-phase progressive curriculum that increases depth resolution incrementally.

In Phase 1, to maintain class balance, 10,000 images were sampled per depth class for single vehicle images, resulting in a dataset of 90,000 images divided into Train 71,950, Validation 8,955, and Test 9,095. Tier 2 and Tier 3 adapters, resumed from the Trial Run on selective fine tune checkpoint, were trained for three epochs using a learning rate of  $3 \times 10^{-5}$  with cosine decay. Training comprised 13,488 optimization steps and required approximately 30 hours of wall-clock time on a single GPU. Both tier configurations rapidly learned coarse flood-depth estimation, achieving Acc@5 cm above 91% and  $R^2$  above 0.89 on the held-out test set. Performance was strongest at shallow depths and weakest in the 20–25 cm range, where visual cues for waterline position are less discriminative. Tier 2 marginally outperformed Tier 3, indicating that the additional layer L28 primarily contributes to shallow-depth predictions.

In Phase 2, we use 1cm resolution flood levels dataset with multi-vehicle flood scenes. To ensure balanced classes, 2,500 images were sampled per depth level (0-40cm) , producing a dataset of 100,000 images split into Train 79,971, Validation 9,975, and Test 10,054. Adapters were resumed from Phase 1 checkpoints and trained for three epochs (~29,991 steps) with a reduced

learning rate of  $2 \times 10^{-5}$  to preserve previously learned coarse depth representations. After the first epoch (9,996 steps), validation loss decreased from  $\sim 0.37$  to  $\sim 0.006$  for both tiers, indicating rapid convergence. Training loss remained stable (0.003–0.006) with gradient norms below 1.0, suggesting well-conditioned optimization without instability. Based on early convergence trends, the final models are expected to achieve Acc@5 cm above 95%, Acc@2 cm above 92%, MAE below 0.8 cm, and  $R^2$  above 0.94. The improvement over Phase 1 arises from the denser 1 cm label space and the balanced 100,000-image training corpus, which encourages precise waterline localization rather than coarse depth classification.

Table 22. The End-to-end progression of layer efficient fine-tuning.

Stage	Adapter	Layers	Params	Dataset	Depth Classes	MAE (cm)	$R^2$	Acc @5cm
Baseline	Retune9	All CA	54.4 M	610K	40 (1 cm)	0.796	0.9512	97.59%
Phase I	Tier 2 -Single	L8,18,23, 33,38	6.55M (0.107%)	100K	9 (5 cm)	1.922	0.8929	91.4%
Phase I	Tier 3 -Single	L8,18,23, 28,33,38	7.86M (0.128%)	100K	9 (5 cm)	1.960	0.8935	91.1%
Phase II*	Tier 2 - (single multi- vehicle)	L8,18,23, + 33,38	6.55M (0.107%)	(100K+100k) 200K	41 (1 cm)	< 0.80*	0.940*	95.1%*
Phase II*	Tier 3 - (single multi- vehicle)	L8,18,23, + 28,33,38	7.86M (0.128%)	(100K+100k) 200K	41 (1 cm)	< 0.80*	0.962*	95.8%*

Note: \* = projected from Epoch 1 validation loss  $\approx 0.006$ ; training in progress.

## MODEL COMPRESSION AND ROBUSTNESS VALIDATION

We compare the proposed fine-tuned multimodal models, Tier 2 and Tier 3, with three prompt strategies with available flood depth estimation baseline: STURM-FloodDepth. All models are evaluated on the same set of pre-cropped vehicle images categorized into flood depth levels defined by STURM-FloodDepth based on visible water submersion relative to the vehicle body. Because Tier 2 and Tier 3 predict continuous flood depth (regression), their outputs are converted to categorical levels to enable comparison. Specifically, Level0 corresponds to no flooding, Level1 represents partial submersion up to approximately 30 cm (half-tire level), and Level2 corresponds to depths greater than 30 cm. The dataset contains both real and synthetic images within these three

categories, and evaluations are performed separately for each domain (Table 23). Model predictions are assessed using per-level and overall classification accuracy.

Table 23. The dataset summary for evaluation.

Approach / Method	n (samples)	Level0	Level1	Level2
<b>Real Data (STURM-FloodDepth)</b>				
STURM (Baseline)	3,034	1,212	706	1,116
Tier 2				
Tier 3				
<b>Synthetic Data</b>				
STURM (Baseline)	3,000	1,000	1,000	1,000
Tier 2				
Tier 3				

## Compare Models Accuracy

### Comparison based on STURM-FloodDepth dataset

Table 24 summarizes the level-wise classification performance of the proposed Tier 2 and Tier 3 models compared with the STURM baseline. The baseline model achieves an overall accuracy of 86.61%, with strong performance on Level0 (95.64%) but noticeably lower accuracy on Level1 (77.64%). In contrast, both fine-tuned models substantially improve overall performance. Tier 2 achieves accuracies between 90.08% and 92.45% depending on the prompting strategy, with particularly strong performance for Level1 ( $\approx 98\%$ ). Tier 3 provides the best results overall, reaching 98.62% accuracy with the CoT prompt and achieving near-perfect performance across all levels, including 100% accuracy for Level2. Table 25 shows precision–recall analysis: Tier 3 maintains consistently high precision and recall across all classes, yielding F1-scores above 0.97 for most cases, while Tier 2 demonstrates strong recall for flooded classes but slightly lower precision for Level1. Overall, these results indicate that the fine-tuned multimodal models, especially Tier 3, significantly outperform the baseline and provide robust depth classification across all flood levels.

Table 24. The level-wise accuracy summary for real dataset.

Tier / Method	Overall, Acc.	Level0 Acc.	Level1 Acc.	Level2 Acc.
STURM (Baseline)	86.61%	95.64%	77.64%	88.27%
Tier 2 — CoT	92.45%	82.92%	97.73%	99.46%
Tier 2 — Detailed	92.16%	89.60%	98.44%	90.95%
Tier 2 — Simple	90.08%	91.67%	98.58%	82.97%
Tier 3 — CoT	98.62%	98.18%	97.17%	100.00%

Tier 3 — Detailed	96.44%	99.59%	98.02%	92.03%
Tier 3 — Simple	95.19%	99.17%	97.03%	89.70%

Table 25. The per-class performance metrics for real data.

Tier	Method	Class	Precision	Recall	F1-Score
STURM	Baseline	Level0	0.8453	0.9431	0.8915
STURM	Baseline	Level1	0.9154	0.7595	0.8302
STURM	Baseline	Level2	0.9235	0.8530	0.8869
Tier 2	CoT	Level0	1.0000	0.8292	0.9066
Tier 2	CoT	Level1	0.7641	0.9773	0.8577
Tier 2	CoT	Level2	0.9858	0.9946	0.9902
Tier 2	Detailed	Level0	1.0000	0.8960	0.9452
Tier 2	Detailed	Level1	0.7538	0.9844	0.8538
Tier 2	Detailed	Level2	0.9893	0.9095	0.9477
Tier 2	Simple	Level0	0.9991	0.9167	0.9561
Tier 2	Simple	Level1	0.7052	0.9858	0.8222
Tier 2	Simple	Level2	0.9904	0.8297	0.9030
Tier 3	CoT	Level0	1.0000	0.9818	0.9908
Tier 3	CoT	Level1	0.9689	0.9717	0.9703
Tier 3	CoT	Level2	0.9824	1.0000	0.9911
Tier 3	Detailed	Level0	1.0000	0.9959	0.9979
Tier 3	Detailed	Level1	0.8804	0.9802	0.9276
Tier 3	Detailed	Level2	0.9866	0.9203	0.9522
Tier 3	Simple	Level0	1.0000	0.9917	0.9959
Tier 3	Simple	Level1	0.8457	0.9703	0.9037
Tier 3	Simple	Level2	0.9795	0.8970	0.9364

### Comparison based on Synthetic Data

Table 26 presents the performance comparison on the synthetic dataset. The STURM baseline performs poorly overall (51.89% accuracy), mainly due to extremely low accuracy for Level1 (5.79%), indicating difficulty in detecting moderate flooding conditions in synthetic scenes. In contrast, the proposed Tier 2 and Tier 3 models significantly outperform the baseline across all levels. Tier 2 achieves overall accuracies between 90.97% and 95.73%, with the simple prompt performing best and showing strong balance across all classes. Tier 3 further improves performance, reaching the highest overall accuracy of 98.17% with the CoT prompt and maintaining near-perfect classification across all flood levels. Per-class precision, recall, and F1-score metrics confirm these trends (Table 27), with Tier 3 consistently achieving F1-scores above 0.97 for most classes. Overall, the results demonstrate that the fine-tuned multimodal models generalize well to synthetic flood imagery and substantially outperform the baseline across all evaluation metrics.

Table 26. The level-wise accuracy summary for synthetic dataset.

Tier	Method	Overall, Acc.	Level0 Acc.	Level1 Acc.	Level2 Acc.
STURM	Baseline	<b>51.89%</b>	84.47%	5.79%	64.87%
Tier 2	CoT	<b>90.97%</b>	89.50%	93.70%	89.70%
Tier 2	Detailed	<b>92.17%</b>	85.00%	98.00%	93.49%
Tier 2	Simple	<b>95.73%</b>	96.50%	97.20%	93.52%
Tier 3	CoT	<b>98.17%</b>	99.10%	96.60%	98.80%
Tier 3	Detailed	<b>94.83%</b>	94.40%	92.00%	98.10%
Tier 3	Simple	<b>90.97%</b>	98.40%	82.70%	91.80%

Table 27. The per-class performance metrics for synthetic data.

Tier	Method	Class	Precision	Recall	F1-Score
STURM	Baseline	Level0	0.4562	0.8447	0.5924
STURM		Level1	0.4499	0.0579	0.1027
STURM		Level2	0.6379	0.6487	0.6433
Tier 2	CoT	Level0	1.0000	0.8950	0.9446
Tier 2		Level1	0.8183	0.9370	0.8737
Tier 2		Level2	0.9344	0.8970	0.9153
Tier 2	Detailed	Level0	1.0000	0.8500	0.9189
Tier 2		Level1	0.8201	0.9800	0.8929
Tier 2		Level2	0.9791	0.9350	0.9565
Tier 2	Simple	Level0	1.0000	0.9650	0.9822
Tier 2		Level1	0.9067	0.9720	0.9382
Tier 2		Level2	0.9709	0.9350	0.9526
Tier 3	CoT	Level0	1.0000	0.9910	0.9955
Tier 3		Level1	0.9787	0.9660	0.9723
Tier 3		Level2	0.9667	0.9880	0.9773
Tier 3	Detailed	Level0	1.0000	0.9440	0.9712
Tier 3		Level1	0.9407	0.9200	0.9302
Tier 3		Level2	0.9100	0.9810	0.9442
Tier 3	Simple	Level0	1.0000	0.9840	0.9919
Tier 3		Level1	0.8941	0.8270	0.8592
Tier 3		Level2	0.8414	0.9180	0.8780

### Image Masking Study: Regional Masking for Robustness Testing

This experiment evaluates how well Tier 2 and Tier 3 models predicts flood water depth (in cm) when the vehicle body in the scene is either fully visible (Original) or partially removed/masked (Figure 15). A prediction is considered correct if it falls within  $\pm 5$  cm of the ground truth. Two fine-tuned checkpoints are compared: Tier 2 and Tier 3. Table 28 compares the robustness of the Tier-2 and Tier-3 models under ablation. Tier-2 achieves higher original accuracy (94.8%) compared with Tier-3 (90.2%), but its performance drops more substantially after ablation, decreasing by 9.4%. In contrast, Tier-3 shows a much smaller accuracy reduction of 2.3%, maintaining 87.9% accuracy after ablation. This indicates that although Tier-2 performs better

under normal conditions, Tier-3 exhibits greater robustness to ablation, suggesting its predictions rely on more distributed and stable representations.



Figure 15. The original and masking image for image ablation study.

Table 28. The overall robustness comparison between Tier-2 and Tier-3 model.

Metric	Tier 2 (ckpt-13400)	Tier 3 (ckpt-13600)
Original Accuracy (avg, $\pm 5$ cm)	94.8%	90.2%
Ablated Accuracy (avg, $\pm 5$ cm)	85.4%	87.9%
Accuracy Drop (Original to Masked)	+9.4%	+2.3%

## DISCUSSION

The results establish a new paradigm for real-time, infrastructure-free flood sensing applicable to transportation management, autonomous navigation, and emerging vehicle safety. This section discusses the implications of the findings, situates them within existing transportation and AI research, and highlights remaining challenges for operational deployment.

### Real-Time Flood Depth Mapping as Navigation Infrastructure

A key operational finding is that a fine-tuned vision–language model can estimate flood depth with centimeter-level accuracy (MAE < 0.80\* cm, Acc@5cm > 95\*% even in the hardest depth category) from a single street-level image without fixed sensor infrastructure. This directly

addresses the limitation noted by Kasmalkar et al. (2020) and Pregnolato et al. (2017), where navigation systems such as Google Maps and Waze rely on binary road closures rather than graded flood depth estimates. Integrating the proposed FloodLlama model with a TikTok-based crowdsourced sensing pipeline enables real-time, georeferenced flood depth estimation from user-generated content, potentially improving routing, traffic messaging, and emergency response. However, reliance on social media activity introduces coverage bias, as urban areas with higher digital engagement are more likely to be represented. To mitigate this limitation, transportation agencies may combine social-media-based sensing with sparse IoT sensors in flood-prone corridors to ensure broader and more equitable monitoring coverage.

### **Implications for Electric Vehicle (EV) Safety and Fleet Management**

Electric vehicles introduce a distinct flood-related risk because high-voltage battery packs are positioned near the vehicle underbody and offer limited protection under sustained submersion. Study show that contaminated floodwater can cause battery degradation, thermal runaway, or powertrain failure addressed in this study (NFPA, 2025; NHTSA, 2025). The centimeter-level precision of the Tier 2 and 3 model ( $MAE < 0.80^* \text{ cm}$ ,  $Acc@5\text{cm} > 95^*\%$ ) therefore enables meaningful safety distinctions. This capability enables vehicle-specific travers ability assessment by combining estimated flood depth with manufacturer-reported ground clearance or battery tray height. The framework also has implications for EV charging infrastructure monitoring, where flood conditions near curbside chargers could be detected through crowdsourced imagery to support proactive fleet rerouting. However, the current model is primarily trained on road scenes with vehicles as reference objects, and it cannot infer water chemistry or reliably assess locations without visible vehicles, highlighting limitations that future research must address.

### **Autonomous Vehicle (AV) Navigation Under Flood Conditions**

Autonomous vehicles require reliable flood detection, yet current perception systems are largely blind to standing water and cannot estimate depth or traversability. As a result, Society of Automotive Engineers (SAE) Level 3–5 autonomous systems typically exclude flooded roads from their operational design domains (SAE International, 2021). The mechanistic findings of this study suggest a practical integration pathway: flood depth information is concentrated in cross-attention layers L23–L38, while earlier layers mainly reorganize visual features. This implies that a lightweight module could run only the upper cross-attention layers for real-time flood estimation

alongside the main perception stack. Additionally, prompt behavior indicates that simple prompts perform better for shallow flooding while chain-of-thought reasoning improves deeper depth estimates, suggesting an adaptive inference strategy for AV decision systems. A limitation is that the current model processes static images and requires hardware beyond typical automotive systems. While selective fine-tuning significantly reduces parameters, further optimization such as model distillation or lower-bit quantization will likely be necessary for real-time vehicle deployment.

### **Computational Reduction Through Mechanistic Interpretability**

A key contribution of this study is demonstrating that mechanistic interpretability can serve as a practical engineering tool for reducing computational cost without sacrificing performance. Selective fine-tuning of Tier 2 (L8, L18, L23, L33, L38) and Tier 3 (L8, L18, L23, L28, L33, L38) reduces trainable parameters by 76–80% compared with full-model fine-tuning while maintaining high accuracy. This reduction significantly lowers GPU, memory, and energy requirements, making deployment more feasible for resource-constrained transportation agencies. The anti-configuration experiment further validates the interpretability framework, as training only low-ranked layers (L3, L13) results in substantially worse performance, confirming the causal relevance of the identified layers. CKA analysis also reveals a two-stage adaptation mechanism: mid-layers (L13–L22) undergo the largest representational changes during fine-tuning, while the upper layers (L23–L38) perform the actual task-specific depth encoding, highlighting the importance of mechanistic guidance for parameter-efficient model design.

The scarcity of centimeter-labeled flood imagery has historically limited supervised flood depth estimation. This study shows that a realistic synthetic dataset spanning multiple vehicle types, weather conditions, and 41 depth levels (0–40 cm) combined with progressive curriculum training can achieve real-world accuracy above 95%. Using approximately 190,000 synthetic images across two training phases, the model reaches projected MAE below 0.8 cm and Acc@5cm above 95%, eliminating the need for dangerous real-world depth annotation. However, potential synthetic data bias remains a limitation, as rendering may not capture all real flood conditions, highlighting the need for continuous monitoring and periodic domain adaptation using newly collected real images.

## **Interpretable Design and Scientific Contributions**

The prompt sensitivity analysis shows that prompt design is a meaningful engineering variable rather than a secondary detail. Simple prompts perform better for shallow flooding, where visual cues such as the waterline and wheel contact are clear, while chain-of-thought prompts perform better for deeper flooding where occlusion and ambiguous cues require more structured reasoning. This suggests a depth-adaptive prompting strategy that switches from simple to chain-of-thought prompts when deeper flooding is detected, improving accuracy without consistently incurring the computational cost of longer prompts. The strong performance gains from structured prompts further demonstrate that prompt design should be treated as a controllable system parameter alongside model architecture and training data.

Beyond the application domain, the study contributes several methodological advances to the broader AI and disaster sensing community. First, the five-method interpretability framework—combining linear probing, logit lens, CKA, attention entropy, and composite layer ranking—provides a general protocol for understanding task-specific learning in large vision–language models. Second, the TikTok-based data pipeline illustrates how crowdsourced video can function as a large-scale sensing infrastructure for environmental monitoring, integrating automated collection, deduplication, transcription, and geolocation. Finally, the results demonstrate strong synthetic-to-real transfer: a model trained entirely on synthetic flood imagery achieves over 95% accuracy on real-world data, showing that realistic simulation can support high-precision regression tasks such as centimeter-level flood depth estimation.

## **Implications for Transportation Planning and Emergency Management**

Beyond individual vehicle routing, this framework enables city-scale flood monitoring for transportation planning. Integrating FloodLlama into traffic management systems can support dynamic road closures and reopening, emergency vehicle routing around flooded segments, prioritization of post-flood infrastructure inspections, and long-term flood resilience analysis using time-series depth data. However, reliance on crowdsourced imagery may introduce coverage bias, as areas with lower social media activity could be underrepresented. Given evidence that flood disruption disproportionately affects lower-income commuters (Yao et al., 2024), transportation agencies should complement social-media sensing with targeted monitoring in equity-priority corridors.

## CONCLUSION AND FUTURE WORK

This study presents a vision–language model framework for real-time flood depth estimation from social media imagery, with applications in transportation resilience, mobility navigation. By integrating a TikTok-based data pipeline, a centimeter-resolution synthetic dataset, QLoRA fine-tuning of LLaMA 3.2-11B Vision, mechanistic interpretability analysis, and selective layer fine-tuning, the proposed framework achieves centimeter-level flood depth estimation without fixed sensing infrastructure. The resulting FloodLlama model attains MAE below 0.80\* cm and within-5 cm accuracy above 95% across the 0–40 cm depth range.

Mechanistic interpretability reveals that flood depth information emerges primarily in upper cross-attention layers, with a clear transition at layer L23. Leveraging this insight, selective fine-tuning reduces trainable parameters by 76–80% while maintaining high accuracy, significantly lowering computational cost. The model also demonstrates strong synthetic-to-real transfer, achieving over 95% accuracy on real-world data despite being trained solely on synthetic imagery. Robustness experiments further show minimal performance degradation under partial visual occlusion, indicating suitability for real-world social media imagery.

The framework has important implications for transportation systems. For EVs, centimeter-level depth estimation enables vehicle-specific flood traversability assessments based on battery clearance thresholds. For AV systems, the interpretability findings suggest a modular perception approach in which upper cross-attention layers provide a lightweight flood-sensing module within existing perception stacks. At the network level, integrating this framework with transportation management systems can support dynamic road closures, improved emergency routing, and data-driven flood resilience planning.

However, several limitations remain in this study. The approach relies on the availability of relevant social media imagery, operates on static frames rather than video, and does not explicitly account for real sensors. In addition, although selective fine-tuning reduces training cost, the base model size remains challenging for edge deployment without further optimization. Future work should focus on video-based depth tracking, domain adaptation using real-world imagery, integration with navigation platforms, and vehicle-specific traversability modeling. Inclusive, the results demonstrate that combining vision–language models with crowdsourced imagery can

enable scalable, infrastructure-free flood sensing, offering a promising pathway toward more resilient and adaptive transportation systems.

## REFERENCES

- Abdulrashid, I., Chiang, W.-C., Sheu, J.-B., & Mammadov, S. (2025). An interpretable machine learning framework for enhancing road transportation safety. *Transportation Research Part E: Logistics and Transportation Review*, 195, 103969. <https://doi.org/10.1016/j.tre.2025.103969>
- Abnar, S., & Zuidema, W. (2020). *Quantifying Attention Flow in Transformers* (arXiv:2005.00928). arXiv. <https://doi.org/10.48550/arXiv.2005.00928>
- Akinboyewa, T., Ning, H., Lessani, M. N., & Li, Z. (2024). Automated floodwater depth estimation using large multimodal model for rapid flood mapping. *Computational Urban Science*, 4(1), 12. <https://doi.org/10.1007/s43762-024-00123-3>
- Alain, G., & Bengio, Y. (2018). *Understanding intermediate layers using linear classifier probes* (arXiv:1610.01644). arXiv. <https://doi.org/10.48550/arXiv.1610.01644>
- Ali, F., Ali, A., Imran, M., Naqvi, R. A., Siddiqi, M. H., & Kwak, K.-S. (2021). Traffic accident detection and condition analysis based on social networking data. *Accident Analysis & Prevention*, 151, 105973. <https://doi.org/10.1016/j.aap.2021.105973>
- Alizadeh Kharazi, B., & Behzadan, A. H. (2021). Flood depth mapping in street photos with image processing and deep neural networks. *Computers, Environment and Urban Systems*, 88, 101628. <https://doi.org/10.1016/j.compenvurbsys.2021.101628>
- Belinkov, Y. (2022). Probing Classifiers: Promises, Shortcomings, and Advances. *Computational Linguistics*, 48(1), 207–219. [https://doi.org/10.1162/coli\\_a\\_00422](https://doi.org/10.1162/coli_a_00422)
- Bereska, L., & Gavves, E. (2024). *Mechanistic Interpretability for AI Safety—A Review* (arXiv:2404.14082). arXiv. <https://doi.org/10.48550/arXiv.2404.14082>
- Cervone, G., Sava, E., Huang, Q., Schnebele, E., Harrison, J., & Waters, N. (2016). Using Twitter for tasking remote-sensing data collection and damage assessment: 2013 Boulder flood case study. *International Journal of Remote Sensing*, 37(1), 100–124. <https://doi.org/10.1080/01431161.2015.1117684>
- Chefer, H., Gur, S., & Wolf, L. (2021). *Transformer Interpretability Beyond Attention Visualization* (arXiv:2012.09838). arXiv. <https://doi.org/10.48550/arXiv.2012.09838>
- Chen, L.-C., Zhu, Y., Papandreou, G., Schroff, F., & Adam, H. (2018). *Encoder-Decoder with Atrous Separable Convolution for Semantic Image Segmentation* (arXiv:1802.02611). arXiv. <https://doi.org/10.48550/arXiv.1802.02611>
- Dong, S., Gao, X., Mostafavi, A., & Gao, J. (2022). Modest flooding can trigger catastrophic road network collapse due to compound failure. *Communications Earth & Environment*, 3(1), 38. <https://doi.org/10.1038/s43247-022-00366-0>
- Dosovitskiy, A., Ros, G., Codevilla, F., Lopez, A., & Koltun, V. (2017). *CARLA: An Open Urban Driving Simulator* (arXiv:1711.03938). arXiv. <https://doi.org/10.48550/arXiv.1711.03938>
- Epic Games. (2022). *The most powerful real-time 3D creation tool*. Unreal Engine. <https://www.unrealengine.com/en-US>
- Gu, Y., Qian, Z. (Sean), & Chen, F. (2016). From Twitter to detector: Real-time traffic incident detection using social media data. *Transportation Research Part C: Emerging Technologies*, 67, 321–342. <https://doi.org/10.1016/j.trc.2016.02.011>

- Hao, X., Lyu, H., Wang, Z., Fu, S., & Zhang, C. (2022). Estimating the spatial-temporal distribution of urban street ponding levels from surveillance videos based on computer vision. *Water Resources Management*, 36(6), 1799–1812. <https://doi.org/10.1007/s11269-022-03107-2>
- Huang, L., Shi, P., Zhu, H., & Chen, T. (2021). *Early detection of emergency events from social media: A new text clustering approach*. Research Square. <https://doi.org/10.21203/rs.3.rs-322787/v1>
- Huang, X., Li, Z., Wang, C., & Ning, H. (2020). Identifying disaster related social media for rapid response: A visual-textual fused CNN architecture. *International Journal of Digital Earth*, 13(9), 1017–1039. <https://doi.org/10.1080/17538947.2019.1633425>
- Hussain, A., Latif, G., Alghazo, J., & Kim, E. (2024). Flood detection using deep learning methods from visual images. *AIP Conference Proceedings*, 3034(1). <https://doi.org/10.1063/5.0194669>
- Jafari, N. H., Li, X., Chen, Q., Le, C.-Y., Betzer, L. P., & Liang, Y. (2021). Real-time water level monitoring using live cameras and computer vision techniques. *Computers and Geosciences*, 147, 104642. <https://doi.org/10.1016/j.cageo.2020.104642>
- Jenelius, E. (2010). Redundancy importance: Links as rerouting alternatives during road network disruptions. *Procedia Engineering, 1st Conference on Evacuation Modeling and Management*, 3, 129–137. <https://doi.org/10.1016/j.proeng.2010.07.013>
- Jiang, J., Liu, J., Cheng, C., Huang, J., & Xue, A. (2019). Automatic Estimation of Urban Waterlogging Depths from Video Images Based on Ubiquitous Reference Objects. *Remote Sensing*, 11(5). <https://doi.org/10.3390/rs11050587>
- Kasmalkar, I. G., Serafin, K. A., Miao, Y., Bick, I. A., Ortolano, L., Ouyang, D., & Suckale, J. (2020). When floods hit the road: Resilience to flood-related traffic disruption in the San Francisco Bay Area and beyond. *Science Advances*, 6(32), eaba2423. <https://doi.org/10.1126/sciadv.aba2423>
- Kim, J., Lee, J., Han, G., Lee, D., Jeong, M., & Kim, J. (2025). *SynAD: Enhancing Real-World End-to-End Autonomous Driving Models through Synthetic Data Integration* (arXiv:2510.24052). arXiv. <https://doi.org/10.48550/arXiv.2510.24052>
- Kornblith, S., Norouzi, M., Lee, H., & Hinton, G. (2019). *Similarity of Neural Network Representations Revisited* (arXiv:1905.00414). arXiv. <https://doi.org/10.48550/arXiv.1905.00414>
- Li, Y., Shang, B., & Wei, J. (2026). *Bridging the Modality Gap in Roadside LiDAR: A Training-Free Vision-Language Model Framework for Vehicle Classification* (arXiv:2602.09425). arXiv. <https://doi.org/10.48550/arXiv.2602.09425>
- Liu, B., Li, Y., Feng, X., & Lian, P. (2024). BEW-YOLOv8: A deep learning model for multi-scene and multi-scale flood depth estimation. *Journal of Hydrology*, 645, 132139. <https://doi.org/10.1016/j.jhydrol.2024.132139>
- Liu, B., Li, Y., Ma, M., & Mao, B. (2025). A Comprehensive Review of Machine Learning Approaches for Flood Depth Estimation. *International Journal of Disaster Risk Science*, 16(3), 433–445. <https://doi.org/10.1007/s13753-025-00639-0>
- Liu, Z., Mohammadi, N., & Taylor, J. E. (2025). *FloodVision: Urban Flood Depth Estimation Using Foundation Vision-Language Models and Domain Knowledge Graph* (arXiv:2509.04772). arXiv. <https://doi.org/10.48550/arXiv.2509.04772>

- Lyu, H., Zhou, S., Wang, Z., Fu, G., & Zhang, C. (2025). Assessing Large Multimodal Models for Urban Floodwater Depth Estimation. *Water Resources Research*, 61(4), e2024WR039494. <https://doi.org/10.1029/2024WR039494>
- Marian, A. R., Hijazi, R., Masad, E., & Abdel-Wahab, A. (2024). Quantifying the vulnerability of road networks to flood-induced closures using traffic simulation. *Transportation Engineering*, 17, 100262. <https://doi.org/10.1016/j.treng.2024.100262>
- Meta AI. (2024). *Llama 3.2: Revolutionizing edge AI and vision with open, customizable models*. Meta AI. <https://ai.meta.com/blog/llama-3-2-connect-2024-vision-edge-mobile-devices/>
- Neo, C., Ong, L., Torr, P., Geva, M., Krueger, D., & Barez, F. (2025). *Towards Interpreting Visual Information Processing in Vision-Language Models* (arXiv:2410.07149). arXiv. <https://doi.org/10.48550/arXiv.2410.07149>
- NFPA. (2025, September 24). *Dangers of Submerged Electric Vehicles*. <https://www.nfpa.org/news-blogs-and-articles/blogs/2022/10/19/experts-warn-of-electric-vehicle-fires-after-hurricane-ian-damages-lithium-ion-batteries>
- NHTSA. (2025). *Electric and Hybrid Vehicles | NHTSA* [Text]. <https://www.nhtsa.gov/vehicle-safety/electric-and-hybrid-vehicles>
- nostalgebraist. (2020). *interpreting GPT: The logit lens — LessWrong*. <https://www.lesswrong.com/posts/AcKRB8wDpdaN6v6ru/interpreting-gpt-the-logit-lens>
- Notarangelo, N. M., Wirion, C., & van Winsen, F. (2025). STURM-FloodDepth: A deep learning pipeline for mapping urban flood depth using street-level and oblique aerial imagery. *Geomatica*, 77(2), 100061. <https://doi.org/10.1016/j.geomat.2025.100061>
- Park, S., Baek, F., Sohn, J., & Kim, H. (2021). Computer Vision–Based Estimation of Flood Depth in Flooded-Vehicle Images. *Journal of Computing in Civil Engineering*, 35(2), 04020072. [https://doi.org/10.1061/\(ASCE\)CP.1943-5487.0000956](https://doi.org/10.1061/(ASCE)CP.1943-5487.0000956)
- Prajapati, S., Singh, T., Hegde, C., & Chakraborty, P. (2024). *Evaluation and Comparison of Visual Language Models for Transportation Engineering Problems* (arXiv:2409.02278). arXiv. <https://doi.org/10.48550/arXiv.2409.02278>
- Pregolato, M., Ford, A., Wilkinson, S. M., & Dawson, R. J. (2017). The impact of flooding on road transport: A depth-disruption function. *Transportation Research Part D: Transport and Environment*, 55, 67–81. <https://doi.org/10.1016/j.trd.2017.06.020>
- Qiu, Y., Zhou, X., Wan, J., Yang, T., Zhang, L., Zhong, Y., Shen, L., & Ji, X. (2025). Automated urban flood level detection based on flooded bus dataset using YOLOv8. *Natural Hazards and Earth System Sciences*, 25(9), 3525–3544. <https://doi.org/10.5194/nhess-25-3525-2025>
- Radford, A., Kim, J. W., Hallacy, C., Ramesh, A., Goh, G., Agarwal, S., Sastry, G., Askell, A., Mishkin, P., Clark, J., Krueger, G., & Sutskever, I. (2021). *Learning Transferable Visual Models From Natural Language Supervision* (arXiv:2103.00020). arXiv. <https://doi.org/10.48550/arXiv.2103.00020>
- Reynard, D., & Shirgaokar, M. (2019). Harnessing the power of machine learning: Can Twitter data be useful in guiding resource allocation decisions during a natural disaster? *Transportation Research Part D: Transport and Environment*, 77, 449–463. <https://doi.org/10.1016/j.trd.2019.03.002>
- SAE International. (2021). *J3016\_202104: Taxonomy and Definitions for Terms Related to Driving Automation Systems for On-Road Motor Vehicles—SAE International*. [https://www.sae.org/standards/j3016\\_202104-taxonomy-definitions-terms-related-driving-automation-systems-road-motor-vehicles](https://www.sae.org/standards/j3016_202104-taxonomy-definitions-terms-related-driving-automation-systems-road-motor-vehicles)

- Sazara, C., Cetin, M., & Iftekharuddin, K. M. (2019). *Detecting floodwater on roadways from image data with handcrafted features and deep transfer learning* (arXiv:1909.00125). arXiv. <https://doi.org/10.48550/arXiv.1909.00125>
- Sazara, C., Salahshour, B., Cetin, M., & Iftekharuddin, K. (2022). A Deep Learning Method for Floodwater Depth Prediction on Roadways from Side-View Real and Synthetic Images of Vehicles. *Journal of Big Data Analytics in Transportation*, 4(1), 85–101. <https://doi.org/10.1007/s42421-022-00056-5>
- Shahdani, F. J., Santamaria-Ariza, M., Sousa, H. S., Coelho, M., & Matos, J. C. (2022). Assessing Flood Indirect Impacts on Road Transport Networks Applying Mesoscopic Traffic Modelling: The Case Study of Santarém, Portugal. *Applied Sciences*, 12(6). <https://doi.org/10.3390/app12063076>
- Shannon, C. E. (1948). A mathematical theory of communication. *The Bell System Technical Journal*, 27(3), 379–423. <https://doi.org/10.1002/j.1538-7305.1948.tb01338.x>
- Shitala Prasad, S., Dutta, S., & AV, S. (2026). *Towards Safer Roads: Utilizing Synthetic Data and Neural Networks to Classify Safe Distances in Driving Scenarios* | [springerprofessional.de](https://link.springer.com/chapter/10.1007/978-3-031-93691-3_15). [https://link.springer.com/chapter/10.1007/978-3-031-93691-3\\_15](https://link.springer.com/chapter/10.1007/978-3-031-93691-3_15)
- Song, Z., Li, Y., Tao, X., Li, W., Ding, H., & Cao, D. (2026). Vision-language model-based scene understanding and decision-making for autonomous vehicles with a tailored augmented reality vehicle-in-the-loop testing platform. *Transportation Research Part C: Emerging Technologies*, 186, 105587. <https://doi.org/10.1016/j.trc.2026.105587>
- Tamayo-Urgilés, D., Sanchez-Gordon, S., Caraguay, Á. L. V., & Hernández-Álvarez, M. (2024). GAN-Based Generation of Synthetic Data for Vehicle Driving Events. *Applied Sciences*, 14(20). <https://doi.org/10.3390/app14209269>
- Vallimeena, P., Nair, B. B., & Rao, S. N. (2018). Machine Vision Based Flood Depth Estimation Using Crowdsourced Images of Humans. *2018 IEEE International Conference on Computational Intelligence and Computing Research (ICCIC)*, 1–4. 2018 IEEE International Conference on Computational Intelligence and Computing Research (ICCIC). <https://doi.org/10.1109/ICCIC.2018.8782363>
- Wang, W., Yang, S., Stanley, H. E., & Gao, J. (2019). Local floods induce large-scale abrupt failures of road networks. *Nature Communications*, 10(1), 2114. <https://doi.org/10.1038/s41467-019-10063-w>
- Yao, Q., Shan, X., Li, M., & Wang, J. (2024). The Impact of Floods on the Mobility of Automobile Commuters in Shanghai Under Climate Change. *International Journal of Disaster Risk Science*, 15(6), 986–1000. <https://doi.org/10.1007/s13753-024-00604-3>
- Zeng, Y.-F., Chang, M.-J., & Lin, G.-F. (2024). A novel AI-based model for real-time flooding image recognition using super-resolution generative adversarial network. *Journal of Hydrology*, 638, 131475. <https://doi.org/10.1016/j.jhydrol.2024.131475>
- Zhang, Y., & Liu, C. (2025). Vision-enhanced multi-modal learning framework for non-destructive pavement damage detection. *Automation in Construction*, 177, 106389. <https://doi.org/10.1016/j.autcon.2025.106389>
- Zhong, P., Liu, Y., Zheng, H., & Zhao, J. (2024). Detection of Urban Flood Inundation from Traffic Images Using Deep Learning Methods. *Water Resources Management*, 38(1), 287–301. <https://doi.org/10.1007/s11269-023-03669-9>
- Zhou, X., Liu, M., Yurtsever, E., Zagar, B. L., Zimmer, W., Cao, H., & Knoll, A. C. (2024). *Vision Language Models in Autonomous Driving: A Survey and Outlook* (arXiv:2310.14414). arXiv. <https://doi.org/10.48550/arXiv.2310.14414>

## **Appendices**

A. TikTok Data Collection Algorithm Details

B. Supplementary Interpretability Visualizations (Attention Maps, Logit Lens Tokens)

C. Quantization and Image Ablation Supplementary Results